ALMA Survey of Orion Planck Galactic Cold Clumps (ALMASOP). II. Survey Overview: A First Look at 1.3 mm Continuum Maps and Molecular Outflows

Somnath Dutta[1], Chin-Fei Lee[1], Tie Liu[2,3], Naomi Hirano[1], Sheng-Yuan Liu[1], Ken'ichi Tatematsu[4,5], Kee-Tae Kim[6,7], Hsien Shang[1], Dipen Sahu[1], Gwanjeong Kim[4], Anthony Moraghan[1], Kai-Syun Jhan[1], Shih-Ying Hsu[1], Neal J. Evans[8], Doug Johnstone[9,10], Derek Ward-Thompson[11], Yi-Jehng Kuan[12,1], Chang Won Lee[6,7], Jeong-Eun Lee[13], Alessio Traficante[14], Mika Juvela[15], Charlotte Vastel[16], Qizhou Zhang[17], Patricio Sanhueza[5,18], Archana Soam[19], Woojin Kwon[20,6], Leonardo Bronfman[21], David Eden[22], Paul F. Goldsmith[23], Jinhua He[21,24,25], Yuefang Wu[26], Veli-Matti Pelkonen[27], Sheng-Li Qin[28], Shanghuo Li[6], and Di Li[29,30]

[1] Institute of Astronomy and Astrophysics, Academia Sinica, Roosevelt Rd, Taipei 10617, Taiwan, R.O.C.; sdutta@asiaa.sinica.edu.tw
[2] Shanghai Astronomical Observatory, Chinese Academy of Sciences, 80 Nandan Road, Shanghai 200030, People's Republic of China; liutie@shao.ac.cn
[3] Key Laboratory for Research in Galaxies and Cosmology, Chinese Academy of Sciences, 80 Nandan Road, Shanghai 200030, People's Republic of China
[4] Nobeyama Radio Observatory, National Astronomical Observatory of Japan, National Institutes of Natural Sciences, 462-2 Nobeyama, Minamimaki, Minamisaku, Nagano 384-1305, Japan
[5] Department of Astronomical Science, SOKENDAI (The Graduate University for Advanced Studies), 2-21-1 Osawa, Mitaka, Tokyo 181-8588, Japan
[6] Korea Astronomy and Space Science Institute (KASI), 776 Daedeokdae-ro, Yuseong-gu, Daejeon 34055, Republic of Korea
[7] University of Science and Technology, Korea (UST), 217 Gajeong-ro, Yuseong-gu, Daejeon 34113, Republic of Korea
[8] Department of Astronomy, The University of Texas at Austin, 2515 Speedway, Stop C1400 Austin, TX 78712-1205, USA
[9] NRC Herzberg Astronomy and Astrophysics, 5071 West Saanich Rd., Victoria, BC V9E 2E7, Canada
[10] Department of Physics and Astronomy, University of Victoria, Victoria, BC V8P 5C2, Canada
[11] Jeremiah Horrocks Institute, University of Central Lancashire, Preston PR1 2HE, UK
[12] Department of Earth Sciences, National Taiwan Normal University, Taipei, Taiwan, R.O.C.
[13] School of Space Research, Kyung Hee University, Yongin-Si, Gyeonggi-Do 17104, Republic of Korea
[14] IAPS-INAF, via Fosso del Cavaliere 100, I-00133, Rome, Italy
[15] Department of Physics, P.O. Box 64, FI-00014, University of Helsinki, Finland
[16] IRAP, Université de Toulouse, CNRS, UPS, CNES, F-31400, Toulouse, France
[17] Center for Astrophysics | Harvard & Smithsonian, 60 Garden Street, Cambridge, MA 02138, USA
[18] National Astronomical Observatory of Japan, National Institutes of Natural Sciences, 2-21-1 Osawa, Mitaka, Tokyo 181-8588, Japan
[19] SOFIA Science Center, Universities Space Research Association, NASA Ames Research Center, Moffett Field, CA 94035, USA
[20] Department of Earth Science Education, Seoul National University, 1 Gwanak-ro, Gwanak-gu, Seoul 08826, Republic of Korea
[21] Departamento de Astronomía, Universidad de Chile, Casilla 36-D, Santiago, Chile
[22] Astrophysics Research Institute, Liverpool John Moores University, IC2, Liverpool Science Park, 146 Brownlow Hill, Liverpool, L3 5RF, UK
[23] Jet Propulsion Laboratory, California Institute of Technology, 4800 Oak Grove Drive, Pasadena, CA 91109, USA
[24] Yunnan Observatories, Chinese Academy of Sciences, 396 Yangfangwang, Guandu District, Kunming, 650216, People's Republic of China
[25] Chinese Academy of Sciences South America Center for Astronomy, National Astronomical Observatories, CAS, Beijing 100101, People's Republic of China
[26] Department of Astronomy, Peking University, 100871 Beijing, People's Republic of China
[27] Institut de Ciències del Cosmos, Universitat de Barcelona, IEEC-UB, Martí i Franquès 1, E-08028 Barcelona, Spain
[28] Department of Astronomy, Yunnan University, and Key Laboratory of Particle Astrophysics of Yunnan Province, Kunming, 650091, People's Republic of China
[29] National Astronomical Observatories, Chinese Academy of Sciences, Beijing 100101, People's Republic of China
[30] NAOC-UKZN Computational Astrophysics Centre, University of KwaZulu-Natal, Durban 4000, South Africa

Abstract

Planck Galactic Cold Clumps (PGCCs) are considered to be the ideal targets to probe the early phases of star formation. We have conducted a survey of 72 young dense cores inside PGCCs in the Orion complex with the Atacama Large Millimeter/submillimeter Array (ALMA) at 1.3 mm (band 6) using three different configurations (resolutions $\sim 0\farcs35$, $1\farcs0$, and $7\farcs0$) to statistically investigate their evolutionary stages and substructures. We have obtained images of the 1.3 mm continuum and molecular line emission (^{12}CO, and SiO) at an angular resolution of $\sim 0\farcs35$ (~ 140 au) with the combined arrays. We find 70 substructures within 48 detected dense cores with median dust mass $\sim 0.093\,M_\odot$ and deconvolved size $\sim 0\farcs27$. Dense substructures are clearly detected within the central 1000 au of four candidate prestellar cores. The sizes and masses of the substructures in continuum emission are found to be significantly reduced with protostellar evolution from Class 0 to Class I. We also study the evolutionary change in the outflow characteristics through the course of protostellar mass accretion. A total of 37 sources exhibit CO outflows, and 20 ($>50\%$) show high-velocity jets in SiO. The CO velocity extents (ΔVs) span from 4 to 110 km s^{-1} with outflow cavity opening angle width at 400 au ranging from $[\Theta_{\rm obs}]_{400} \sim 0\farcs6$–$3\farcs9$, which corresponds to $33\fdg4$–$125\fdg7$. For the majority of the outflow sources, the ΔVs show a positive correlation with $[\Theta_{\rm obs}]_{400}$, suggesting that as protostars undergo gravitational collapse, the cavity opening of a protostellar outflow widens and the protostars possibly generate more energetic outflows.

1. Introduction

Stars form within dense cores (typical size ~0.1 pc, density ~10^4 cm^{-3}, and temperature ~10 K) in the clumpy and filamentary environment of molecular clouds (Myers & Benson 1983; Williams et al. 2000). In past decades, observations revealed the presence of embedded protostars within dense cores, which has also led to the classification of "prestellar" and "protostellar" phases of dense cores (Beichman et al. 1986; Bergin & Tafalla 2007). The puzzle begins with the understanding of how a prestellar core condenses to form a star or multiple system and how a protostar accumulates its central mass from the surrounding medium during its evolution. Studies of extremely young dense cores at different evolutionary phases offer the best opportunity to probe the core formation under diverse environmental conditions, as well as determine the transition phase from prestellar to protostellar cores, study protostellar evolution, and investigate the outflow/jet launching scenario and physical changes with the protostellar evolution.

In addition, a significant fraction of stars are found in multiple systems. Thus, our understanding of star formation must account for the formation of multiple systems. In one popular star formation theory, the "turbulent fragmentation" theory, turbulent fluctuations in a dense core become Jeans unstable and collapse faster than the background core (e.g., Padoan & Nordlund 2002; Fisher 2004; Goodwin et al. 2004), forming multiple systems. Turbulent fragmentation is likely the dominant mechanism for wide binary systems (Chen et al. 2013; Tobin et al. 2016b; Lee et al. 2017b). Observations indicate that the multiplicity fraction and the companion star fraction are highest in Class 0 protostars and decrease in more evolved protostars (Chen et al. 2013; Tobin et al. 2016b), confirming that multiple systems form in the very early phase.

The "turbulent fragmentation" theory predicts that the fragmentation begins in the starless core stage (Offner et al. 2010). Small-scale fragmentation/coalescence processes have been detected within 0.1 pc scale regions of some starless cores in nearby molecular clouds (Ohashi et al. 2018; Tatematsu et al. 2020; Tokuda et al. 2020). To shed light on the formation of multiple stellar systems, however, we ultimately need to study the internal structure and gas motions within the central 1000 au of starless cores. Over the past few years, several attempts have been made to detect the very central regions and possible substructures of starless cores (e.g., Schnee et al. 2010, 2012; Dunham et al. 2016; Kirk et al. 2017; Caselli et al. 2019). However, no positive results regarding the fragmentation within the central 1000 au of starless cores have been collected so far. Probing substructures of a statistically significant sample of starless cores at the same distance will put this theoretical paradigm ("turbulent fragmentation") to a stringent observational test. If no substructure is detected, this will raise serious questions to our current understanding of this framework. Irrespective of the theoretical framework, these observations will empirically constrain, at high resolution, the starless core structure at or near collapse.

After the onset of star formation, a (Keplerian) rotating disk is formed, feeding a central protostar. However, the detailed process of the disk formation and evolution (growth) is unclear. In theory, material in a collapsing core will be guided by magnetic field lines toward the midplane, forming an infalling-rotating flattened envelope called a "pseudodisk" (Galli & Shu 1993a, 1993b; Allen et al. 2003). A rotating disk is then formed in the innermost (<100 au) part of the pseudodisk. In the pseudodisk, magnetic braking may be efficient, affecting the formation and growth of the disk (Galli et al. 2006). Therefore, high-resolution (×10 au) dust polarization and molecular line observations of Class 0 protostars (the youngest known accreting protostars) and their natal cores are key to constrain theoretical models for the formation of protostellar disks by unveiling their magnetic fields and gas kinematics.

However, disks in young Class 0 protostars have largely remained elusive to date. We have lacked the observational facilities capable of probing this regime in these extremely young objects. As a consequence, we do not know when disks form or what they look like at formation. Recently, large high-resolution continuum surveys have revealed several tens of Class 0 disk candidates (Tobin et al. 2020). So far, however, only several Class 0 protostars (e.g., VLA 1623, HH 212, L 1527, and L 1448-NB) have been suggested to harbor Keplerian-like kinematics at scales $40 < r < 100$ au (Murillo et al. 2013; Codella et al. 2014; Ohashi et al. 2014; Tobin et al. 2016a). The most convincing case for a resolved Class 0 protostellar disk was found in the HH 212 Class 0 protostar, evidenced by an equatorial dark dust lane with a radius of ~60 au at submillimeter wavelengths (Lee et al. 2017a). A systematic high-resolution continuum (polarization) and molecular line survey of Class 0 protostars is urgently needed to search for more Class 0 disk candidates and study disk formation. Collimated bipolar outflows together with fattened continuum emission (pseudodisk) can help identify Class 0 disk candidates.

Low-velocity bipolar outflows are nearly ubiquitous in accreting, rotating, and magnetized protostellar systems (Snell et al. 1980; Cabrit & Bertout 1992; Bontemps et al. 1996; Dunham et al. 2014; Yıldız et al. 2015; Kim et al. 2019). The lower transitions of CO are the most useful tracers of molecular outflows because their low energy levels are easily populated by collisions with H_2 and He molecules at the typical densities and temperatures of molecular clouds (Bally 2016; Lee 2020). The outflows appear as bipolar from the polar regions along the axis of rotation at the early collapsing phase within the pseudodisk (Larson 1969), and remain active throughout the journey of protostellar accretion (Bate 1998; Masunaga & Inutsuka 2000; Tomisaka 2002; Machida et al. 2014; Lee 2020). As protostars evolve, the physical properties of outflow components diversify significantly based on the natal environment. Both numerical simulations and observations have revealed that the opening angle of the outflow cavity widens with time as more material is evacuated from the polar region and the equatorial pseudodisk grows (Shang et al. 2006; Arce et al. 2007; Seale & Looney 2008; Frank et al. 2014; Kuiper et al. 2016). Typically, sources in the Class 0 phase exhibit CO outflow opening angles of 20°–50°, which increase for Class I (80°–120°) and Class II (100°–160°). The outflow velocity is also expected to increase with time as the mass loss increases with accretion rate (Hartigan & Hillenbrand 2009; Bally 2016).

A significant number of Class 0, I, and early II protostars are observed to exhibit extremely high-velocity (EHV) collimated molecular jets (or typically high-density knots) within the wide-angle low-velocity outflow cavities. These high-velocity jets mainly originate from the inner edges of the disk, and jet velocities increase with the evolutionary stage of the protostars in the range of ~100 to a few hundred km s^{-1} in the later phases (Anglada et al. 2007; Hartigan et al. 2011; Machida & Basu 2019). The gas content of the jets also transitions from predominantly molecular to mostly atomic (Bally 2016; Lee 2020). The jets in the younger sources, like Class 0, are mainly detectable in molecular gas, e.g., CO, SiO, and SO at (sub)millimeter and H_2 in the infrared wavelength. Conversely, in the older population like evolved Class I and Class II

sources, the jets are mainly traceable in atomic and ionized gas, e.g., O I, Hα, and S II (Reipurth & Bally 2001; Bally 2016; Lee 2020).

To summarize, more high-resolution observations are needed to study the fragmentation and structures (e.g., disks, outflows) of dense cores in the earliest phases of star formation, i.e., from prestellar cores to the youngest protostellar (Class 0) cores.

1.1. Observations of Planck Galactic Cold Clumps in the Orion Complex

The low dust temperatures (∼14 K) of the Planck Galactic Cold Clumps (PGCCs) make them ideal targets for investigating the initial conditions of star formation (Planck Collaboration et al. 2016). Through observations of ∼1000 PGCCs in the JCMT large survey program "SCOPE: SCUBA-2 Continuum Observations of Pre-protostellar Evolution" (PI: Tie Liu), we have cataloged nearly 3500 cold ($T_d \sim 6$–20 K) dense cores, most of which are either starless or in the earliest phase of star formation (Liu et al. 2018; Eden et al. 2019). This sample of "SCOPE" dense cores represents a real goldmine for investigations of the very early phases of star formation.

The Orion complex contains the nearest giant molecular clouds (GMCs) that harbor high-mass star formation sites. As a part of the SCOPE survey, all the dense PGCCs (average column density $>5 \times 10^{20}$ cm^{-2}) of the Orion complex (Orion A, B, and λ Orionis GMCs) were observed at 850 μm using the SCUBA-2 instrument at the JCMT 15 m telescope (Liu et al. 2018; Yi et al. 2018). A total of 119 dense cores were revealed inside these PGCCs, which includes protostars and gravitationally unstable starless cores (Yi et al. 2018). This sample represents the dense cores of mass spectrum in the range 0.2–14 $M_\odot$, with a median mass of ∼1.4 $M_\odot$ and mean radius ∼0.05 pc as estimated from SCUBA-2 850 μm continuum observations (Yi et al. 2018). Their centrally peaked emission features in the SCUBA-2 850 μm continuum attribute them to likely be gravitationally unstable and possibly headed for imminent collapse (Ward-Thompson et al. 2016).

These Orion dense cores were further investigated in multiple molecular lines (e.g., N$_2$D$^+$, DCO$^+$, DNC in $J = 1$–0 transitions) with the NRO 45 m telescope (Kim et al. 2020; Tatematsu et al. 2020). This follow-up molecular line survey toward 113 of these 119 SCUBA-2 objects with the Nobeyama Radio Observatory (NRO) 45 m telescope revealed nearly half of these SCUBA-2 objects showing strong emission from young, cold, and dense gas tracers, such as N$_2$D$^+$, DCO$^+$, DNC (Kim et al. 2020; Tatematsu et al. 2020).

In particular, high spatial resolution observations with interferometers have already reported very young stellar objects inside some of these SCUBA-2 dense cores. With the Submillimeter Array (SMA), Liu et al. (2016) reported the detection of an extremely young Class 0 protostellar object and a proto-brown dwarf candidate in the bright-rimmed clump PGCC G192.32-11.88 located in the λ Orionis cloud. Very recently, Tatematsu et al. (2020) observed a star-forming core (PGCC G210.82-19.47 North1; hereafter, G210) and a starless core (PGCC G211.16-19.33 North3; hereafter, G211) in the Orion A cloud with the 7 m Array of the Atacama Compact Array (ACA) of the Atacama Large Millimeter/submillimeter Array (ALMA). The two cores show a relatively high deuterium fraction in single-pointing observations with the Nobeyama 45 m radio telescope. In ACA observations, the starless core G211 shows a clumpy structure with several

subcores, which in turn show chemical differences. In contrast, the star-forming core G210 shows an interesting spatial feature of two N$_2$D$^+$ peaks of similar intensity and radial velocity located symmetrically with respect to the single dust continuum peak, suggesting the existence of an edge-on pseudo-disk.

All of the previous observations indicate that those Orion SCUBA-2 cores inside PGCCs are ideal for investigating the initial conditions of star formation in a GMC environment.

1.2. ALMASOP: ALMA Survey of Orion PGCCs

In ALMA cycle 6, we initiated a survey-type project, the ALMA Survey of Orion PGCCs (ALMASOP), to systematically investigate the fragmentation of starless cores and young protostellar cores in Orion PGCCs with ALMA. We selected 72 extremely cold young dense cores from Yi et al. (2018), including 23 starless core candidates and 49 protostellar core candidates. We call them candidates because they were classified mainly based on the four Wide-field Infrared Survey Explorer (WISE) bands (3.4–22 μm) in Yi et al. (2018). In this work, we will further classify them with all available infrared data (e.g., Spitzer, Herschel) as well as our new ALMA data. All 23 starless core candidates of this sample show high-intensity N$_2$D$^+$(1–0) emission with peak brightness temperature higher than 0.2 K in 45 m NRO observations (Kim et al. 2020; Tatematsu et al. 2020), a signpost for the presence of a dense core on the verge of star formation. Intense N$_2$D$^+$ emission was also observed in 21 protostellar core candidates (Kim et al. 2020; Tatematsu et al. 2020). The remaining 28 protostellar core candidates were not detected in N$_2$D$^+$ (Kim et al. 2020; Tatematsu et al. 2020), suggesting they are more evolved than those detected in N$_2$D$^+$. These dense cores, therefore, design a unique sample to probe the onset of star formation and the early evolution of dense cores. The observed target names and coordinates are listed in columns 1, 2, and 3, respectively, in Table 1, and their spatial distribution is shown in Figure 1.

In this paper, we present an overview of the ALMASOP survey, including the observations and data products, along with mostly qualitative previews of the results from forthcoming papers. We have incorporated some perspectives of detection of multiplicity in protostellar systems and the physical characteristics of their outflow lobes. More detailed quantitative results regarding multiplicity formation in the prestellar to protostellar phases, outflow and jet characteristics, disk formation, and astrochemical changes from the prestellar to protostellar phases will be presented in forthcoming papers. Section 2 discusses the details of the observations with regard to the survey and data analyses. In Section 3, the science goals and early results of this survey are described. Section 4 delineates the discussion on the evolution of dense cores and protostellar outflows. Section 5 presents a summary and the conclusions of this study.

2. Observations

The ALMA observations of ALMASOP (Project ID:2018.1.00302.S.; PI: Tie Liu) were carried out with ALMA band 6 in Cycle 6 toward the 72 extremely young dense cores, during 2018 October to 2019 January. The observations were executed in four blocks in three different array configurations: 12 m C43-5 (TM1), 12 m C43-2 (TM2), and 7 m ACA. The execution blocks, date of observations, array configurations,

Table 1
Details of Targeted Dense Cores in the Orion Complex

ALMA Targets (1)	R.A. (J2000) (h:m:s) (2)	Decl. (J2000) (d:m:s) (3)	JCMT Name (4)	Detection (TM1+TM2+ACA) (5)	rms (mJy beam^{-1}) (6)	Detection (ACA only) (7)	rms (mJy beam^{-1}) (8)
			λ-Orionis				
G191.90-11.21N	05:31:28.99	+12:58:47.16	G191.90-11.21N	NO	0.03	NO (weak?)	0.24
G191.90-11.21S	05:31:31.73	+12:56:14.99	G191.90-11.21S	YES	0.04	YES	3.3
G192.12-11.10	05:32:19.54	+12:49:40.19	G192.12-11.10	YES	0.06	YES	2.1
G192.32-11.88N	05:29:54.47	+12:16:56	G192.32-11.88N	YES	0.08	YES	1.0
G192.32-11.88S	05:29:54.74	+12:16:32	G192.32-11.88S	YES	0.03	YES	1.0
G196.92-10.37	05:44:29.6	+09:08:54	G196.92-10.37	YES	0.04	YES	1.8
G198.69-09.12N1	05:52:29.61	+08:15:37	G198.69-09.12N1	NO	0.06	NO	0.3
G198.69-09.12N2	05:52:25.3	+08:15:09	G198.69-09.12N2	NO	0.06	NO (weak?)	0.4
G200.34-10.97N	05:49:03.71	+05:57:56	G200.34-10.97N	YES	0.04	YES	1.0
			Orion A				
G207.36-19.82N1	05:30:50.94	−04:10:35.6	G207.36-19.82N1	YES	0.06	YES	1.2
G207.36-19.82N2	05:30:50.853	−04:10:13.641	G207.36-19.82N2	NO	0.04	YES	1.2
G207.36-19.82N4	05:30:44.546	−04:10:27.384	G207.36-19.82N4	NO (weak?)	0.035	YES	0.5
G207.36-19.82S	05:30:47.199	−04:12:29.734	G207.36-19.82S	NO	0.04	NO	0.4
G208.68-19.20N1	05:35:23.486	−05:01:31.583	G208.68-19.20N1	YES	0.45	YES	4.0
G208.68-19.20N2	05:35:20.469	−05:00:50.394	G208.68-19.20N2	YES	0.14	YES	6.0
G208.68-19.20N3	05:35:18.02	−05:00:20.7	G208.68-19.20N3	YES	0.2	YES	6.0
G208.68-19.20S	05:35:26.32	−05:03:54.393	G208.68-19.20S	YES	0.1	YES	7.0
G208.89-20.04E	05:32:48.262	−05:34:44.335	G208.89-20.04E	YES	0.1	YES	2.5
G208.89-20.04Walma[a]	05:32:28.03	−05:34:26.69	⋯	YES	0.04	YES	1.8
G209.29-19.65N1	05:35:00.379	−05:39:59.741	G209.29-19.65N1	NO (weak?)	0.04	YES (weak?)	2.2
G209.29-19.65S1	05:34:55.991	−05:46:04	G209.29-19.65S1	YES	0.05	YES	3.3
G209.29-19.65S2	05:34:53.809	−05:46:17.627	G209.29-19.65S2	NO (weak?)	0.04	NO (weak?)	1.5
G209.55-19.68N1	05:35:08.9	−05:55:54.4	G209.55-19.68N1	YES	0.09	YES	4.0
G209.55-19.68N2	05:35:07.5	−05:56:42.4	G209.55-19.68N2	NO (weak?)	0.04	YES	0.9
G209.55-19.68S1	05:35:13.476	−05:57:58.646	G209.55-19.68S1	YES	0.2	YES	4.2
G209.55-19.68S2	05:35:09.076	−05:58:27.378	G209.55-19.68S3[b]	YES	0.08	YES	1.9
G209.77-19.40E2	05:36:31.977	−06:02:03.765	G209.77-19.40E2	NO	0.05	NO	0.5
G209.77-19.40E3	05:36:35.9	−06:02:42.165	G209.77-19.40E3	NO	0.04	YES	0.7
G209.79-19.80W	05:35:10.696	−06:13:59.318	G209.79-19.80W	NO	0.04	NO (weak?)	0.7
G209.94-19.52N	05:36:11.55	−06:10:44.76	G209.94-19.52N	NO (weak?)	0.09	YES	2.0
G209.94-19.52S1	05:36:24.96	−06:14:04.71	G209.94-19.52S1	NO	0.05	YES (weak?)	1.0
G210.37-19.53N	05:36:55.03	−06:34:33.19	G210.37-19.53N	NO	0.04	YES	1.0
G210.37-19.53S	05:37:00.55	−06:37:10.16	G210.37-19.53S	YES	0.05	YES	2.3
G210.49-19.79W	05:36:18.86	−06:45:28.035	G210.49-19.79W	YES	0.7	YES	4.0
G210.82-19.47N2	05:37:59.989	−06:57:15.462	G210.82-19.47N2	NO (weak?)	0.05	YES	1.0
G210.82-19.47S	05:38:03.677	−06:58:24.141	G210.82-19.47S	YES	0.07	YES	0.5
G210.97-19.33S2	05:38:45.3	−07:01:04.41	G210.97-19.33S2	YES	0.05	YES	1.0
G211.01-19.54N	05:37:57.469	−07:06:59.068	G211.01-19.54N	YES	0.07	YES	2.3
G211.01-19.54S	05:37:59.007	−07:07:28.772	G211.01-19.54S	YES	0.05	YES	0.8
G211.16-19.33N2	05:39:05.831	−07:10:41.515	G211.16-19.33N2	YES	0.04	YES	0.5
G211.16-19.33N4	05:38:55.68	−07:11:25.9	G211.16-19.33N4	NO	0.05	YES (weak)	0.7
G211.16-19.33N5	05:38:46	−07:10:41.9	G211.16-19.33N5	NO (other?)	0.07	YES	0.7
G211.47-19.27N	05:39:57.18	−07:29:36.082	G211.47-19.27N	YES (Close Binary?)	0.12	YES	2.0
G211.47-19.27S	05:39:56.097	−07:30:28.403	G211.47-19.27S	YES	0.25	YES	11.0
G211.72-19.25S1alma[a]	05:40:21.21	−07:36:08.79	⋯	NO	0.05	NO	1.0
G212.10-19.15N1	05:41:21.34	−07:52:26.92	G212.10-19.15N1	YES	0.04	YES	1.0
G212.10-19.15N2	05:41:24.03	−07:53:47.51	G212.10-19.15N2	YES	0.04	YES	1.0
G212.10-19.15S	05:41:26.446	−07:56:52.547	G212.10-19.15S	YES	0.25	YES	3.0
G212.84-19.45N	05:41:32.146	−08:40:10.45	G212.84-19.45N	YES	0.12	YES (weak?)	4.5
G215.44-16.38	05:56:58.45	−09:32:42.3	G215.44-16.38	NO	0.04	YES (weak?)	0.7
G215.87-17.62M	05:53:32.4	−10:25:05.99	G215.87-17.62M	YES	0.04	YES	2.0
G215.87-17.62N	05:53:41.89	−10:24:02	G215.87-17.62N	YES	0.04	YES	0.8
G215.87-17.62S	05:53:26.249	−10:27:29.473	G215.87-17.62S	NO (other?)	0.04	YES (weak?)	0.8
			Orion B				
G201.52-11.08	05:50:59.01	+04:53:53.1	G201.52-11.08	YES	0.03	YES	0.5
G203.21-11.20E1	05:53:51.004	+03:23:07.3	G203.21-11.20E1	NO (weak?)	0.03	YES	1.0
G203.21-11.20E2	05:53:47.483	+03:23:11.3	G203.21-11.20E2	NO	0.04	NO (weak?)	0.4

Table 1
(Continued)

ALMA Targets (1)	R.A. (J2000) (h:m:s) (2)	Decl. (J2000) (d:m:s) (3)	JCMT Name (4)	Detection (TM1+TM2+ACA) (5)	rms (mJy beam^{-1}) (6)	Detection (ACA only) (7)	rms (mJy beam^{-1}) (8)
G203.21-11.20W1	05:53:42.702	+03:22:35.3	G203.21-11.20W1	YES	0.04	YES	3.0
G203.21-11.20W2	05:53:39.492	+03:22:24.9	G203.21-11.20W2	YES	0.04	YES	0.3
G205.46-14.56M1	05:46:08.053	−00:10:43.712	G205.46-14.56N3[b]	YES	0.5	YES	2.0
G205.46-14.56M2	05:46:07.9	−00:10:01.82	G205.46-14.56N2[b]	YES	0.08	YES	2.0
G205.46-14.56M3	05:46:05.66	−00:09:33.64	G205.46-14.56N1[b]	YES	0.05	YES	1.0
G205.46-14.56N1	05:46:09.75	−00:12:16.45	G205.46-14.56M1[b]	YES	0.15	YES	1.0
G205.46-14.56N2	05:46:07.4	−00:12:21.84	G205.46-14.56M2[b]	YES	0.15	YES	2.5
G205.46-14.56S1	05:46:07.048	−00:13:37.777	G205.46-14.56S1	YES	0.15	YES	4.0
G205.46-14.56S2	05:46:04.49	−00:14:18.81	G205.46-14.56S2	YES	0.08	YES	1.5
G205.46-14.56S3	05:46:03.385	−00:14:51.715	G205.46-14.56S3	YES	0.06	YES	2.0
G206.12-15.76	05:42:45.358	−01:16:13.262	G206.12-15.76	YES	0.3	YES	12.0
G206.21-16.17N	05:41:39.544	−01:35:52.212	G206.21-16.17N	NO (weak?)	0.04	YES	1.0
G206.21-16.17S	05:41:36.373	−01:37:43.61	G206.21-16.17S	NO (weak?)	0.03	YES	0.4
G206.93-16.61E2	05:41:37.31	−02:17:18.135	G206.93-16.61E2	YES	0.15	YES	4.0
G206.93-16.61W2	05:41:25.132	−02:18:06.455	G206.93-16.61W3[b]	YES	0.15	YES	10.0
G206.93-16.61W4	05:41:28.77	−02:20:04.3	G206.93-16.61W5[b]	NO	0.04	NO	3.0

Notes. In column 5 and 7, "*weak*" emission detections are marked, whereas the $\sim 3\sigma$ level emissions or questionable detections are marked with "*weak?*". These are not included in the final detection count. In a few targeted positions, no emission was detected around the dense core coordinates but some other compact emission was detected; these cases are marked with "*other?*".
[a] In the ALMA archive, they are listed as G208.89-20.04W, and G211.72-19.25S1, respectively. These objects are different than the JCMT dense cores cataloged in Yi et al. (2018) with the same names. These objects are selected directly from JCMT images for ALMA observations.
[b] Note that the ALMA archive names are different than the JCMT dense core names in Yi et al. (2018).

(This table is available in machine-readable form.)

number of antennas, exposure times on the targets, and unprojected baselines are listed in Table 2. For observations in the C43-5, C43-2, and compact 7 m ACA, the unprojected baseline lengths range from 15–1398, 15–500, and 9–49 m, respectively. The resulting maximum recoverable scale was 25″.

The ALMA band 6 receivers were utilized to simultaneously capture four spectral windows (SPWs), as summarized by the correlator setup in Table 3. The ALMA correlator was configured to cover several main targeted molecular line transitions (e.g., $J = 2–1$ of CO and $C^{18}O$; $J = 3–2$ of N_2D^+, DCO^+, and DCN; and SiO $J = 5–4$) simultaneously. A total bandwidth of 1.875 GHz was set up for all SPWs. The velocity resolution is about 1.5 km s^{-1}. Different quasars were observed to calibrate the bandpass, flux, and phase, as tabulated in Table 4 with their flux densities.

In this paper, we present the results of the cold dusty envelope+disk emission tracer 1.3 mm continuum, low-velocity outflow tracer CO $J = 2–1$ (230.462 GHz), and high-velocity jet tracer SiO $J = 5–4$ (217.033 GHz) line emission. The acquired visibility data were calibrated using the standard pipeline in CASA 5.4 (McMullin et al. 2007) for different scheduling blocks (SB) separately. We then separated visibilities for all 72 sources, each with their three different observed configurations. For each source, we generated both 1.3 mm continuum and spectral visibilities by selecting all line-free channels, fitting, and subtracting continuum emission in the visibility domain. Imaging of the visibility data was performed with the TCLEAN task in CASA 5.4, using a threshold of 3σ theoretical sensitivity and the "hogbom" deconvolver. We applied Briggs weighting with robust +2.0 (natural weighting) to obtain a high-sensitivity map that best

suits the weak emission at the outer envelope, and it does not degrade the resolution much in comparison with robust +0.5. We generated two sets of continuum images. One set includes all configurations TM1+TM2+ACA to obtain continuum maps with a synthesized beam of $\sim 0\rlap{.}''38 \times 0\rlap{.}''33$ and typical sensitivity ranging from 0.01 to 0.2 mJy beam^{-1}; the TM1 and TM2 configurations contribute to improving the resolution, and the compact ACA configuration improves the missing flux problem. For the large-scale structures, we also obtained a second set of continuum images from only the 7 m ACA configuration visibilities with a synthesized beam of $7\rlap{.}''6 \times 4\rlap{.}''1$ and typical sensitivity of 0.6–2.0 mJy beam^{-1}. The detections of dense cores are listed in combined configurations (column 5) with rms (column 6), plus in ACA only (column 7) with rms (column 8), in Table 1.

On the other hand, since CO $J = 2–1$ and SiO $J = 5–4$ emission are strong, a robust weighting factor of +0.5 was used to generate CO and SiO channel maps using a combination of three visibilities (i.e., TM1+TM2+ACA) with typical synthesized beam sizes of $\sim 0\rlap{.}''41 \times 0\rlap{.}''35$ and $\sim 0\rlap{.}''44 \times 0\rlap{.}''37$, respectively. We binned the channels with a velocity resolution of 2 km s^{-1} to improve the signal-to-noise ratio (S/N), and thus we obtained typical sensitivity ranging 0.02–0.2 mJy beam^{-1}.

3. Science Goals and Early Results

3.1. Continuum Emission at 1.3 mm

The main science goal of the ALMASOP project is to study the fragmentation of these extremely young dense cores with high resolution 1.3 mm continuum data from ALMA. We will investigate the substructures of starless cores and the multi-plicities of protostellar cores. In this work, we only present the
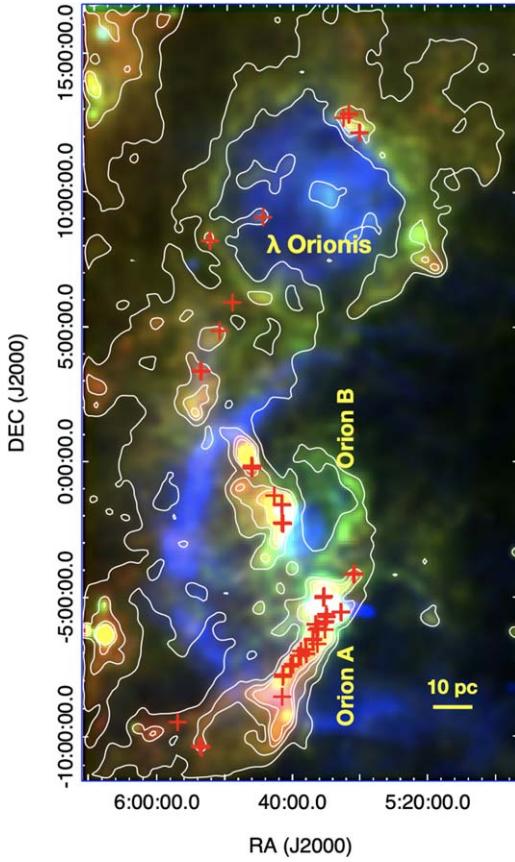
Figure 1. Spatial distribution of the observed cores (red "+") on the three-color composite image (red: Planck 857 GHz; green: IRAS 100 μm; blue: H$_\alpha$) of the Orion complex. Images are smoothed with a Gaussian kernel. White contours represent the flux density of Planck 857 GHz continuum emission. Contour levels are 14.8, 29.7, 44.5, and 59.4 MJy sr^{-1}.

1.3 mm continuum images and briefly discuss the properties of the detected cores. We leave the detailed discussions of the substructures of starless cores and the multiplicities of protostellar cores to forthcoming papers.

Figure 2 shows some selected examples of the 1.3 mm continuum maps toward the dense cores with a typical resolution of $\sim$0$\farcs$35 ($\sim$140 au). The respective continuum maps in each panel reveal diverse morphologies of the dense cores. For example, Figure 2(a) displays 1.3 mm continuum emission of G209.29-19.65S1, which is a candidate prestellar core. It shows an extended envelope that contains a dense blob-like structure. In Figure 2(b), the compact core of G191.90-11.21S is likely a protostar with a much brighter peak than the candidate prestellar core G209.29-19.65S1 (Figure 2(a)), as it is surrounded by extended emission; this source was later classified as Class 0 (Section 3.3). Figure 2(c) contains the compact emission of G205.46-14.56S3 with a relatively fainter surrounding envelope than is typical for Class 0, and this source was later found to be a Class I source (Section 3.3). Some protostellar continuum structures exhibit close multiplicity on the present observed scale, as shown in Figure 2(d).

The full 1.3 mm continuum images for targets in λ-Orionis, Orion A, and Orion B GMCs are presented in the Appendix, in Figures A1, A2, and A3, respectively.

Out of 72 targets, 48 have been detected in the combined three configurations ($\sim$66%), where a total of 70 compact cores have been revealed including the multiple systems. In the other

24 targets, there is either no emission or only 3σ level emission in the combined TM1+TM2+ACA continuum maps, where the dense cores may have sizes larger than the maximum recoverable size (MRS $\sim$ 14$''$) of the combined data, although they could be detected in ACA maps (MRS $\sim$ 25$''$). As an example, Figure 3 (left panel) does not display significant emission in its combined map, although we can see significant emission in ACA only (right panel of Figure 3). Therefore, we checked those targeted positions in ACA only (see Figure A4), which reveals an additional 10 detections ($>5\sigma$). Thus, from the present survey, we are able to detect the emission of 80% of the targeted sources (58 out of 72).

We performed one-component two-dimensional Gaussian fitting in TM1+TM2+ACA maps within the five-sigma contour level to those 70 core structures detected in the combined configurations. Here, we do not compare the measurement from ACA-only detections, due to different resolutions; the results for those ACA configurations will be presented in a separate paper. The fitting parameters are listed in the Table 5, which includes deconvolved major axis, minor axis, position angle, integrated flux density ($F_{1.3\,mm}$), and peak flux (Peak$_{1.3\,mm}$). The source sizes[31] (S_{ab}) were obtained from the geometrical mean of major and minor axes (i.e., $S_{ab} = \sqrt{major \times minor}$).

Assuming optically thin emission, the (gas and dust) mass of the envelope+disk can be roughly estimated using the formula

$$M_{EnvDisk} \sim \frac{D^2 F_\nu}{B_\nu(T_{dust})\kappa_\nu}, \qquad (1)$$

where D is the distance to the sources, which is $\sim$389 $\pm$ 3, 404 $\pm$ 5, and 404 $\pm$ 4 pc for Orion A, Orion B, and λ-Ori sources, respectively (Kounkel et al. 2018). Here, B_ν is the Planck blackbody function at the dust temperature T_{dust}, F_ν is the observed flux density, and κ_ν is the mass opacity per gram of the dust mass. We assume the dust temperature to be 25 K for candidate protostellar disk envelopes[32] (Tobin et al. 2020) and 6.5 K[33] for candidate starless cores (Crapsi et al. 2007; Caselli et al. 2019). Taking a gas-to-dust mass ratio of 100, the theoretical dust mass opacity at 1.3 mm is considered to be $\kappa_\nu = 0.00899(\nu/231\,GHz)^\beta$ cm^2 g^{-1} (Lee et al. 2018) in the early phase for coagulated dust particles with no ice mantles (see also OH5: column 5 of Ossenkopf & Henning (1994)), where we assume the dust opacity spectral index, $\beta = 1.5$ for this size scale. Table 5 lists the estimated masses from these analyses.

Figure 4 (black steps) shows the distribution of all the measured $F_{1.3\,mm}$, $M_{EnvDisk}$, Peak$_{1.3\,mm}$, and S_{ab} with median values of 32.10 mJy, 0.093 $M_\odot$, 14.33 mJy beam^{-1}, and 0$\farcs$27, respectively. More than 80% of this sample have 1.3 mm flux densities $<$100 mJy, peak fluxes $<$50 mJy beam^{-1}, and average sizes $<$0$\farcs$6. Note that the ALMA emission peaks

---

[31] Here, these sizes are analogous to the diameters of the sources.
[32] The protostellar systems may show different dust temperatures of the envelope+disk system based on the stellar luminosity. If these sources also have an extended but colder envelope, the mass of the cold envelope will be underestimated by this assumption of warm temperature. For instance, if we vary the temperature of the protostars from 15 to 100 K, the masses will change by a factor of 1.7–0.25 times the present estimated masses at 25 K.
[33] Due to the heating effect from the environment, the temperature of the starless core is relatively higher ($\sim$10 K) than that of the denser inner part (e.g., Bergin & Tafalla 2007; Sipilä et al. 2019). When the starless cloud collapses and density increases at the central region (as in the prestellar core), then the temperature can reach as low as $\sim$6.5 K at the central dense portion.

Table 2
Log of Observations

Scheduling Block (9)	Number of Execution (10)	Date (11)	(12)	Array Configuration (13)	Number of Antennas (14)	Time on Target (s) (15)	Unprojected Baselines (m) (16)
1	1	2018 Oct 24		C43-5	48	3430	15–1398
	2	2018 Dec 21		C43-2	46	1394	15–500
	3	2018 Nov 19		ACA	12	4590	9–49
2	1	2018 Oct 29		C43-5	47	4569	15–1398
	2	2018 Nov 01		C43-5	44	4654	15–1358
	3	2018 Nov 01		C43-5	44	4655	15–1358
	4	2019 Jan 16		C43-2	46	3542	15–313
	5	2018 Nov 21		ACA	12	5324	9–49
	6	2018 Nov 27		ACA	12	5201	9–49
	7	2018 Nov 27		ACA	12	5185	9–49
	8	2018 Nov 27		ACA	12	5320	9–49
	9	2018 Nov 28		ACA	11	5200	9–49
3	1	2018 Oct 29		C43-5	47	1918	15–1398
	2	2019 Mar 05		C43-2	48	1086	15–360
	3	2018 Nov 21		ACA	12	2634	9–49
	4	2018 Nov 26		ACA	12	2635	9–49
4	1	2018 Oct 25		C43-5	47	3134	15–1398
	2	2019 Jan 24		C43-2	51	1252	15–360
	3	2018 Nov 21		ACA	12	4330	9–49
	4	2018 Nov 26		ACA	12	4048	9–49

Note. This table is organized according to execution block and array configuration, not with date of observations.

Table 3
Correlator Setup

Spectral Window (6)	Central Frequency (GHz) (7)	Main Molecular Lines (8)	Bandwidth (GHz) (9)	Velocity Resolution (km s^{-1}) (10)
0	231.000000	$^{12}CO\ J = 2-1$; N_2D^+ $J = 3-2$	1.875	1.465
1	233.000000	CH_3OH transitions	1.875	1.453
2	218.917871	$C^{18}O\ J = 2-1$; H_2CO transitions	1.875	1.546
3	216.617675	$SiO\ J = 5-4$; DCN $J = 3-2$; DCO^+ $J = 3-2$	1.875	1.563

(Table 5) are shifted from JCMT peaks (Table 1), mainly due to the resolution difference between the two telescopes.

3.2. Outflow and Jet Profiles

The ALMASOP project will investigate the jet launching mechanisms and the evolution of outflows in the earliest phases, i.e., Class 0 stage, of star formation. Using the $^{12}CO(2-1)$ and $SiO(5-4)$ transitions at $\sim0\farcs35$ (~140 au) angular resolution, we have performed a systematic search for low-velocity outflow components and high-velocity collimated jet components driven by protostellar objects.

3.2.1. Outflow Components from CO Emission

One common way to distinguish young protostars from a sample of the dense cores embedded in the molecular cloud is to identify the molecular outflowing gas in the lower rotational transition ^{12}CO (2–1). We have traced such blue- and redshifted outflow wings through visual inspection of velocity channel maps and their spectra. An example of a bipolar ^{12}CO outflow total intensity map integrated over the full blueshifted and redshifted velocity range is shown in Figure 5 for the source G205.46-14.53S3. The blue- and redshifted components (gray color and black contours) shows V-shaped structures toward the NE and SW directions, respectively. The 1.3 mm continuum (magenta contours) exhibits a compact continuum with its continuum inner core ($>20\sigma$ in Figure 5) nearly elongated in a direction nearly perpendicular to the outflow axis.

The velocity extents of the blue- and redshifted lobes are selected from the channel where they appears for the first time at 3σ level, to the channel of disappearance at the same the 3σ limit (e.g., Cabrit & Bertout 1992; Yıldız et al. 2015). As an example, Figure 6 shows the position–velocity (PV) diagram, derived along the outflow axis. The object systemic velocity is likely 12 ± 4 km s^{-1}. The maximum outflow velocity or extent of the blue component is estimated as $\Delta V_B = 114^{+8}_{-24}$ km s^{-1}, where the redshifted components have a velocity extent of $\Delta V_R = 106^{+8}_{-24}$ km s^{-1}, without any inclination correction. The average velocity extent (ΔV) is estimated from both components. We have identified 37 outflow sources with CO emission wings. The extents of both blue- and redshifted lobes observed in CO are tabulated in Table 5 (see Figure 8). However, these ΔVs are the lower limits in the small field of view (FOV) of our combined configuration maps, and we do not know the actual spatial extension of the outflow wings. The CO outflow images for all the protostellar samples are shown in Figure A5.

These velocity extents are different for blue- and redshifted lobes with high uncertainties, which could be due to the missing short velocity spacing on both ends of the lobes in the

Table 4
Calibrators and Their Flux Densities

Scheduling Block (6)	Date (7)	Bandpass Calibrator (Quasar, Flux Density) (8)	Flux Calibrator (Quasar, Flux Density) (9)	Phase Calibrator (Quasar, Flux Density) (10)
1	2018 Oct 24	J0423−0120, 2.68 Jy	J0423−0120, 2.68 Jy	J0607−0834, 0.78 Jy
	2018 Dec 21	J0522−3627, 3.65 Jy	J0522−3627, 3.65 Jy	J0542−0913, 0.47 Jy
	2018 Nov 19	J0522−3627, 4.91 Jy	J0522−3627, 4.91 Jy	J0607−0834, 0.78 Jy
2	2018 Oct 29	J0423−0120, 2.53 Jy	J0423−0120, 2.53 Jy	J0541−0211, 0.095 Jy
	2018 Nov 01	J0423−0120, 2.53 Jy	J0423−0120, 2.53 Jy	J0541−0211, 0.095 Jy
	2018 Nov 01	J0423−0120, 2.53 Jy	J0423−0120, 2.53 Jy	J0541−0211, 0.095 Jy
	2019 Jan 16	J0522−3627, 3.14 Jy	J0522−3627, 3.14 Jy	J0542−0913, 0.47 Jy
	2018 Nov 21	J0854+2006, 2.77 Jy	J0854+2006, 2.77 Jy	J0607−0834, 0.78 Jy
	2018 Nov 27	J0423−0120, 2.30 Jy	J0423−0120, 2.30 Jy	J0542−0913, 0.47 Jy
	2018 Nov 27	J0522−3627, 4.39 Jy	J0522−3627, 4.39 Jy	J0542−0913, 0.47 Jy
	2018 Nov 27	J0854+2006, 3.06 Jy	J0854+2006, 3.06 Jy	J0607−0834, 0.78 Jy
	2018 Nov 28	J0423−0120, 2.29 Jy	J0423−0120, 2.29 Jy	J0542−0913, 0.47 Jy
3	2018 Oct 29	J0510+1800, 1.40 Jy	J0510+1800, 1.40 Jy	J0530+1331, 0.31 Jy
	2019 Mar 05	J0750+1231, 0.65 Jy	J0750+1231, 0.65 Jy	J0530+1331, 0.30 Jy
	2018 Nov 21	J0423−0120, 2.40 Jy	J0423−0120, 2.29 Jy	J0530+1331, 0.30 Jy
	2018 Nov 26	J0423−0120, 2.40 Jy	J0423−0120, 2.29 Jy	J0530+1331, 0.30 Jy
4	2018 Oct 25	J0510+1800, 1.54 Jy	J0510+1800, 1.54 Jy	J0552+0313, 0.35 Jy
	2019 Jan 24	J0423−0120, 2.68 Jy	J0423−0120, 2.68 Jy	J0552+0313, 0.35 Jy
	2018 Nov 21	J0522−3627, 5.07 Jy	J0522−3627, 5.07 Jy	J0532+0732, 1.13 Jy
	2018 Nov 26	J0423−0120, 2.40 Jy	J0423−0120, 2.40 Jy	J0532+0732, 1.13 Jy

present poor velocity-resolution observations, unknown inclination angle, complex gas dynamics of ambient clouds, or global infall in the protostar bearing filaments. In some cases, such as G211.01-19.45S, the outflow is identified as monopolar where the other part could be disregarded due to low velocities, or confused with emission from other sources. Estimated ΔVs range from 4–110 km s^{-1}, with a median value 26.5 km s^{-1}. In some cases, complex structures are observed, where it is difficult to distinguish the outflow wings from the complex cloud environment (marked "cx" in Table 5). These sources can not be ruled out from the outflow candidates, and further investigations are needed at high velocity and spatial resolution with numerical analysis to extract their features from the cloud dynamics.

3.2.2. Identification of High-velocity Knots

The large impact of the Orion cloud kinematics on the outflows makes it difficult to elucidate the original outflow morphology in CO(2–1) tracer. SiO(5–4) has been found to provide more insights into the outflow chemistry (Louvet et al. 2016). The excitation conditions of the SiO(5–4) emission line have a high critical density of $(5–10) \times 10^6$ cm^{-3} (Nony et al. 2020), which could be reached in high-density knot components. The collimated jets frequently appear as a series of knots, which are interpreted as made by the internal shocks originated by episodic accretion/ejection at the protostellar mass-loss rate (Bachiller et al. 1991). An example of blue- and redshifted SiO emission is shown in Figure 5. The identification of the jet components is marked in Table 5 (column 14), and these sources are considered as jet sources throughout the paper.

Out of 37 outflow sources, 18 (∼50%) are detected having knots in the SiO line emission within the CO outflow cavities. Additionally, two non-CO-emitting sources are also identified with SiO emission, where CO emission is possibly nondetectable due to complex cloud environment, as discussed above. High-mass molecular clumps are reported to have ∼50%–90% jet detection in low-angular resolution surveys in SiO(2–1), (3–2), (5–4) emission lines (e.g., Csengeri et al. 2016; Li et al. 2019; Nony et al. 2020). It is to be noted that the high-density shock components could also be detected in more high-density tracers, e.g., SiO (8–7). Therefore, the higher transitions of SiO could reveal more knot-ejecting sources. Additionally, the knot tracers may vary with the evolution of the protostars (Lee 2020).

3.2.3. Outflow Opening Angle

Among the main characteristics of outflows, opening angle (α) is one of the less-explored observational parameters to date. In the low-velocity regime, the CO delineates two-cavity walls open in the blue and redshifted directions. Measuring the α is quite complicated for the sources with no well-defined cavity walls throughout the full observed extent due to the presence of a complex cloud environment (e.g., G200.34-10.97N, G205.46-14.56S1, G209.55-19.68S1), or secondary outflows (e.g., G209.55-19.68N1) (see Appendix, Figure A5). For both the blue- and redshifted directions, if the conical structures appear to be symmetrical, then one can find the apex by extrapolating the cavity boundaries (e.g., Wang et al. 2014). However, the real complexity of finding the apex position appears for asymmetrical outflow lobes: even if we assume the continuum peak to be the apex position, the tangent will be needed to allow us to trace back to that apex location. Hence, we may miss a significant fraction of the cavity width near the source. In that case, we also do not know the outflow-launching radius for the source, which essentially varies from source to source. Thus, we adopt a consistent approach for all the sources, where the outflow cavity width (Θ_{obs}) is measured perpendicular to the outflow axis.
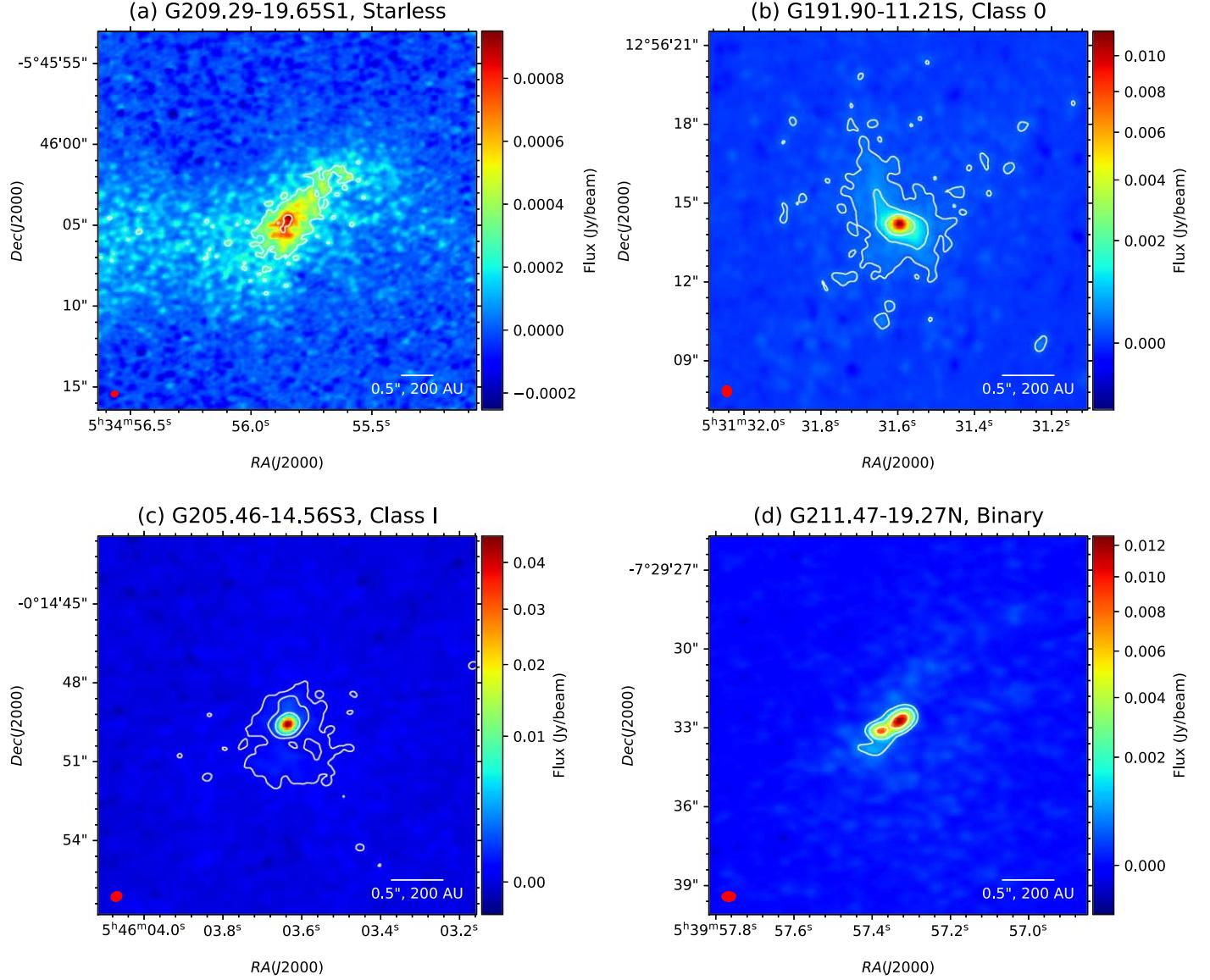
Figure 2. Example images of ALMA 1.3 mm continuum toward selected dense cores. Typical beam sizes $\sim 0\rlap{.}{''}35$ are drawn in the lower left of each panel in red ellipse. Contour levels are at $5 \times (1, 2, 10)\sigma$. Source sequences are: (a) starless core G209.29-19.65S1, where $\sigma = 5 \times 10^{-5}$ Jy beam^{-1}; (b) Class 0 system G191.90-11.21S, where $\sigma = 4 \times 10^{-5}$ Jy beam^{-1}; (c) Class I system G205.46-14.53S3, where $\sigma = 6 \times 10^{-5}$ Jy beam^{-1}; (d) binary system G211.47-19.27N, where $\sigma = 12 \times 10^{-5}$ Jy beam^{-1}. Notice that the extended emission turns more compact as we evolve from starless to Classes 0 and I. Interestingly, the peak emission is also increasing on the same sequence (see text for more details).

First, the outflow axis of each lobe is derived from their knot structures in SiO emission (Figure 5). For the sources having no SiO emission, CO jets are utilized to find the jet axis from the dense CO emission near the middle of the outflow cavity walls. Some of the sources show neither SiO knots nor CO jets; in those cases, their outflow axis was assumed to be in the middle of the outflow cavity. Second, we draw an average tangent at the outermost 3σ contours at the local point of consideration (cyan dashed lines in Figure 5). Now, the width perpendicular to the jet axis of the 3σ cavity wall at $1''$ (i.e., $[\Theta_{\rm obs}]_{400}$ at ~ 400 au; yellow double-headed arrow) and $2''$ (i.e., $[\Theta_{\rm obs}]_{800}$ at ~ 800 au; green double-headed arrow) distance from continuum peak represents the opening angle at the corresponding distance from the stellar core. As shown in the schematic diagram on top of Figure 5, if the opening angle width is measured as $[\Theta_{\rm obs}]_D$ at a distance D from the continuum peak, from right angle trigonometry, the half of

opening angle is $\frac{\alpha}{2} = \tan^{-1}\left(\frac{[\theta_{\rm obs}]_D / 2}{D}\right)$. We also measured $[\theta_{\rm obs}]_D$ at distances $>2''$, and found that α measurements are quite consistent for the outflows with well-defined cavity walls. However, we prefer to present $[\theta_{\rm obs}]_D$ close to the source, i.e., at $1''$ and $2''$, for all the sources in order to minimize the environmental effects on the measurements, and as shown in Figure 7(a) and (b), the overall trends of $[\theta_{\rm obs}]_D$ with $T_{\rm bol}$ remain the same for both the distances. The exact envelope boundaries and other environment effects toward each of the outflow lobes are also unknown, which could lead to unequal deformation on both the outflow lobes. Thus, we have taken an average of blue- and redshifted opening angles to measure the final $\Theta_{\rm obs}$ to reduce the unknown contamination. From the present analyses, we are able to estimate $[\Theta_{\rm obs}]_D$ of 22 outflow sources, and the values of the final $[\Theta_{\rm obs}]_D$ are listed in Table 5. The CO outflow cavities have an opening angle width at $1''$ (~ 400 au) ranging from $0\rlap{.}{''}6$ to $3\rlap{.}{''}9$ (i.e., typically
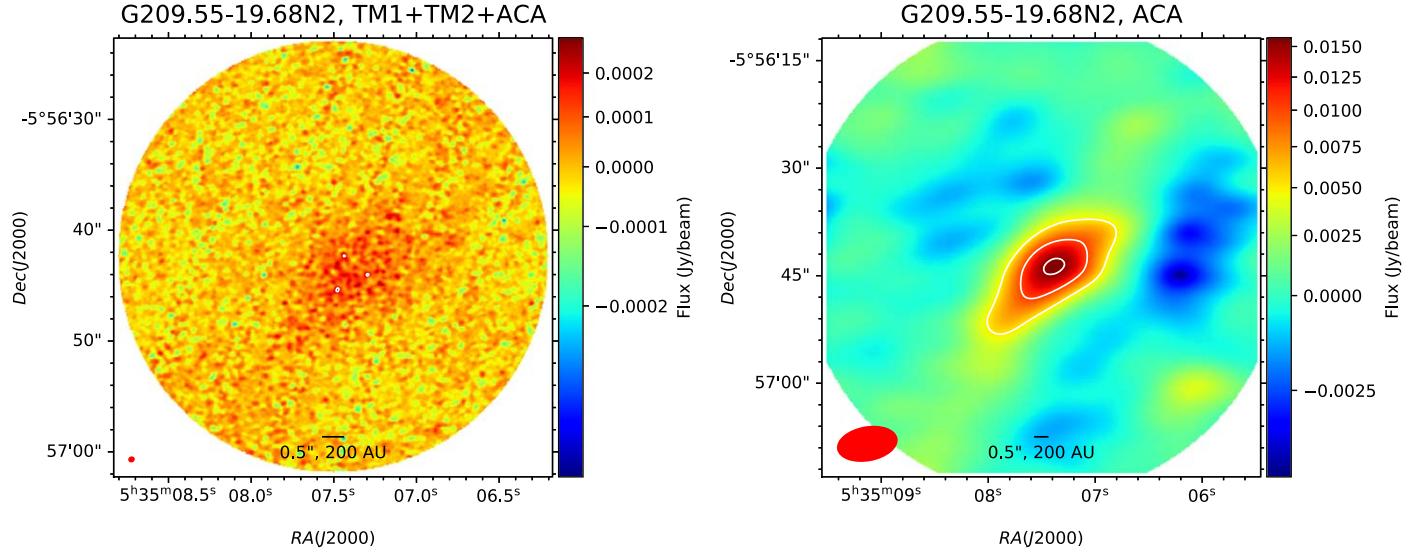
Figure 3. Example images of 1.3 mm continuum observations for combined TM1+TM2+ACA in the left panel, and ACA only in the right panel are shown. Typical beam sizes are shown at the lower left in each panel with the red ellipses. The combined resolution resolved out the emission. A compact structure is clearly seen in ACA only, with contour levels $5 \times (1, 2, 10)\sigma$, where $\sigma = 0.001$ Jy beam^{-1}.

$\alpha = 33°.4$–$125°.7$ near the source) with a median value $1''.64$. The median value for 19 Class 0 sources is $1''.60$ and 3 Class I sources is $2''.70$ (see Section 3.3 for objects classification).

These measured quantities of opening angles are not corrected for inclination angle, i. As in Figure 5, the continuum emission is apparently shifted toward the blueshifted lobes, which is most probably an inclination effect, and at the same distance from the continuum peaks, the blue lobes appear wider than the red lobes. Measuring the inclination angle requires well-defined outflow cavity walls, with their full spatial extent. Therefore, we need high-velocity resolution and wide FOV for the outflows, which we lack in the present data sets. Note that we need to define the exact shell structure in order to estimate the real-age opening angle; for a rotating outflow, it is complex to search the corresponding shell cavity in low-velocity resolution observations. In such cases, we assume the outer boundary as the outflow shell, which introduces error in the Θ_{obs}. Thus, theoretical models are necessary to reduce the environmental effects of complex cloud dynamics, envelope emission, and interacting outflows. Further high-velocity resolution and single-dish observations are also very important to determining the envelope boundary and inclination angle.

3.3. Protostellar Signatures

3.3.1. Multiwavelength Catalog

The surrounding envelopes are dissipated during protostellar evolution. They gradually appear from submm, mid-infrared (MIR) to near-infrared (NIR) wavelengths, hence they become less sensitive to 1.3 mm emission. Thus, we searched for the submm, MIR, and NIR counterparts of each dense core in the archived Two-Micron All-Sky Survey (2MASS; Cutri et al. 2003), UKIRT Infrared Deep Sky Survey (UKIDSS; Lawrence et al. 2007), Spitzer Space Telescope survey of Orion A-B (Megeath et al. 2012), WISE (Wright et al. 2010), AKARI (Doi et al. 2015), Herschel Orion Protostellar survey (HOPS; Stutz et al. 2013; Tobin et al. 2015), Atacama Pathfinder Experiment (APEX; Stutz et al. 2013), and the 850 μm JCMT (Yi et al. 2018). In addition to these catalogs, we include our present ALMA 1.3 mm emission in order to estimate a more accurate bolometric temperature (T_{bol}) and luminosity (L_{bol}) than that of Yi et al. (2018).

The final multiwavelength catalog was obtained by cross-matching all the catalogs described above. Initially, we adopted a matching radius of $r_m \sim 3''$ for all the catalogs (for details, see Dutta et al. (2015)), which best suits the relatively high-resolution catalogs, 2MASS, UKIDSS, Spitzer, and ALMA. For the relatively poor-resolution catalogs, WISE, AKARI, Herschel, APEX, JCMT, we further checked the images within their corresponding resolution limits to consider the counterpart of an object. For the possible close binary in the present analysis, with the available observations, it is difficult to determine the exact source of infrared emission because the binary system is embedded in a common envelope. We therefore assigned the same measurements to both protostars. The final cross-matched catalog is presented in Table 6. Finally, the objects with good photometric accuracy (S/N > 10 for 2MASS, UKIDSS, Spitzer-IRAC and Spitzer-MIPS; S/N > 20 for WISE and ALMA; S/N > 50 for AKARI, JCMT, Herschel, APEX) were utilized for the further analyses (e.g., Dutta et al. 2018). For the HOPS fluxes, we adopted the uncertainty flags as provided in Furlan et al. (2016).

The T_{bol} and L_{bol} were estimated with trapezoid-rule integration over the available fluxes, assuming the distance as $\sim 389 \pm 3$, 404 ± 5, and 404 ± 4 pc for Orion A, Orion B, and λ-Ori sources, respectively (Kounkel et al. 2018), and the measured values are listed in Table 5. Following Myers & Ladd (1993), the flux-weighted mean frequencies in the observed spectral energy distributions (SEDs) were utilized to obtain T_{bol}. We assume $T_{bol} = 70$ K as a quantitative transition temperature from Class 0 to Class I (e.g., Chen et al. 1995). Our distributions of T_{bol} and L_{bol} are close to the measured values of the HOPS catalog (Furlan et al. 2016); the HOPS IDs are marked in column 18 of Table 5. Some differences are expected because we are using (additional) mid-infrared data not included in the HOPS catalog. For some sources, the mid-infrared observations (e.g., AKARI and Herschel) are not available, therefore our measurements should give the lower limit for those sources (Kryukova et al. 2012).

Table 5
Continuum and Emission-line Properties of All Objects

			1.3 mm Continuum (TM1+TM2+ACA)						CO and SiO					Infrared			
Source	R.A.	Decl.	Maj	Min	PA	$F_{1.3\ mm}$	$Peak_{1.3\ mm}$	Mass	ΔV_B	ΔV_R	Θ_{400}	Θ_{800}	SiO[a] (Y/ N)	T_{bol}	L_{bol}	Class[b]	HOPS
	(h:m:s)	(d:m:s)	″	″	(°)	(mJy)	(mJy/beam)	($M_\odot$)	(km s^{-1})	(km s^{-1})	(″)	(″)		(K)	($L_\odot$)		
(1)	(2)	(3)	(4)	(5)	(6)	(7)	(8)	(9)	(10)	(11)	(12)	(13)	(14)	(15)	(16)	(17)	(18)
G191.90-11.21S	05:31:31.60	+12:56:14.15	0.693 ± 0.031	0.395 ± 0.027	79.93 ± 3.76	27.77 ± 1.08	10.11 ± 0.30	0.079 ± 0.034	22^{+10}_{-4}	24^{+8}_{-4}	1.59 ± 0.36	2.28 ± 0.36	Y	69 ± 17	0.4 ± 0.2	0	⋯
G192.12-11.10	05:32:19.37	+12:49:40.92	0.792 ± 0.009	0.276 ± 0.007	121.96 ± 0.52	119.24 ± 1.25	44.32 ± 0.35	0.340 ± 0.145	40^{+8}_{-14}	44^{+8}_{-14}	3.56 ± 0.66	4.46 ± 0.22	N	44 ± 15	9.5 ± 4.0	0	⋯
G192.32-11.88N	05:29:54.15	+12:16:52.99	0.276 ± 0.005	0.237 ± 0.006	65.27 ± 5.77	143.22 ± 0.82	102.72 ± 0.38	0.408 ± 0.174	20^{+8}_{-4}	4^{+10}_{-2}	na	na	N	na	na	0	⋯
G192.32-11.88S	05:29:54.41	+12:16:29.68	5.374 ± 0.361	4.001 ± 0.269	23.85 ± 9.12	34.99 ± 2.35	0.27 ± 0.02	0.100 ± 0.043	cx	cx	na	na	N	60 ± 13	0.1 ± 0.1	0	⋯
G196.92-10.37_A	05:44:29.26	+09:08:52.18	0.459 ± 0.023	0.375 ± 0.022	17.68 ± 13.47	24.06 ± 0.62	12.72 ± 0.23	0.069 ± 0.029	54^{+12}_{-12}	34^{+10}_{-14}	2.71 ± 0.75	4.75 ± 1.30	N	na	na	0	⋯
G196.92-10.37_B	05:44:30.02	+09:08:57.30	0.234 ± 0.011	0.067 ± 0.042	86.46 ± 3.96	14.82 ± 0.16	12.96 ± 0.08	0.042 ± 0.018	na	na	na	na	N	143 ± 28	3.5 ± 2.0	1	⋯
G196.92-10.37_C[c]	05:44:29.98	+09:08:56.25	0.000 ± 0.000	0.000 ± 0.000	0.00 ± 0.00	1.62 ± 0.10	1.84 ± 0.06	0.005 ± 0.002	na	na	na	na	N	143 ± 28	3.5 ± 2.0	1	⋯
G200.34-10.97N	05:49:03.35	+05:57:58.11	0.361 ± 0.011	0.321 ± 0.016	142.61 ± 20.97	23.92 ± 0.42	14.64 ± 0.17	0.068 ± 0.029	18^{+8}_{-6}	14^{+8}_{-4}	0.90 ± 0.14	1.23 ± 0.20	N	43 ± 10	1.5 ± 0.6	0	⋯
G201.52-11.08	05:50:59.15	+04:53:49.65	0.673 ± 0.010	0.182 ± 0.014	124.81 ± 0.80	21.17 ± 0.28	10.02 ± 0.09	0.060 ± 0.026	cx	cx	na	na	N	263 ± 55	0.3 ± 0.2	1	⋯
G203.21-11.20W1	05:53:42.59	+03:22:34.97	0.395 ± 0.010	0.176 ± 0.010	73.37 ± 1.84	32.09 ± 0.40	22.33 ± 0.18	0.091 ± 0.039	12^{+6}_{-8}	12^{+6}_{-6}	0.98 ± 0.15	1.33 ± 0.10	N	na	na	0	⋯
G203.21-11.20W2	05:53:39.51	+03:22:23.85	0.777 ± 0.051	0.430 ± 0.032	64.50 ± 4.50	11.89 ± 0.64	4.16 ± 0.17	0.034 ± 0.015	58^{+14}_{-10}	46^{+16}_{-12}	2.24 ± 0.13	3.27 ± 0.40	Y	15 ± 5	0.5 ± 0.3	0	⋯
G205.46-14.56M1_A	05:46:08.60	−00:10:38.49	0.314 ± 0.052	0.254 ± 0.054	123.35 ± 77.51	22.38 ± 1.58	15.54 ± 0.71	0.064 ± 0.028	46^{+16}_{-16}	30^{+14}_{-14}	na	na	Y	47 ± 12	4.8 ± 2.1	0	317
G205.46-14.56M1_B	05:46:08.38	−00:10:43.54	1.268 ± 0.033	0.582 ± 0.018	84.49 ± 1.25	788.03 ± 19.41	148.79 ± 3.11	2.245 ± 0.960	36^{+14}_{-14}	8^{+10}_{-4}	na	na	N	na	na	0	⋯
G205.46-14.56M2_A	05:46:07.85	−00:10:01.30	0.147 ± 0.027	0.098 ± 0.052	68.01 ± 30.45	12.93 ± 0.26	11.84 ± 0.14	0.037 ± 0.016	na	na	na	na	N	112 ± 27	9.4 ± 3.9	111	387
G205.46-14.56M2_B	05:46:07.84	−00:09:59.60	0.269 ± 0.008	0.121 ± 0.016	40.52 ± 4.64	43.62 ± 0.41	34.70 ± 0.20	0.124 ± 0.053	2^{+4}_{-0}	14^{+12}_{-8}	na	na	N	112 ± 28	9.4 ± 3.9	1	387
G205.46-14.56M2_C	05:46:08.48	−00:10:03.04	0.135 ± 0.009	0.071 ± 0.024	49.23 ± 9.08	31.87 ± 0.25	29.79 ± 0.14	0.091 ± 0.039	cx	cx	na	na	N	163 ± 34	21.0 ± 8.0	111	386
G205.46-14.56M2_D	05:46:08.43	−00:10:00.50	0.569 ± 0.052	0.400 ± 0.051	53.48 ± 13.21	10.00 ± 0.67	4.22 ± 0.21	0.028 ± 0.012	cx	cx	na	na	Y	163 ± 34	21.0 ± 8.0	1	386
G205.46-14.56M2_E	05:46:08.92	−00:09:56.12	0.079 ± 0.053	0.054 ± 0.026	125.45 ± 34.83	3.75 ± 0.12	3.66 ± 0.07	0.011 ± 0.005	na	na	na	na	N	na	na	111	⋯
G205.46-14.56M3	05:46:05.97	−00:09:32.69	5.652 ± 0.247	4.751 ± 0.207	108.72 ± 10.21	55.16 ± 2.40	0.37 ± 0.02	1.240 ± 0.532	na	na	na	na	N	na	na	−1	⋯
G205.46-14.56N1	05:46:10.03	−00:12:16.88	0.382 ± 0.005	0.254 ± 0.006	57.13 ± 1.88	166.75 ± 1.05	103.98 ± 0.44	0.475 ± 0.203	cx	cx	na	na	N	29 ± 8	0.6 ± 0.3	0	402
G205.46-14.56N2	05:46:07.72	−00:12:21.27	0.445 ± 0.009	0.332 ± 0.008	139.79 ± 3.45	78.31 ± 1.01	41.79 ± 0.37	0.223 ± 0.095	cx	cx	na	na	N	32 ± 8	0.8 ± 0.3	0	401
G205.46-14.56S1_A	05:46:07.26	−00:13:30.23	0.374 ± 0.011	0.188 ± 0.014	77.78 ± 2.84	53.17 ± 0.77	36.57 ± 0.34	0.151 ± 0.065	42^{+8}_{-14}	20^{+12}_{-12}	1.36 ± 0.27	1.58 ± 0.65	Y	44 ± 19	22.0 ± 8.0	0	358
G205.46-14.56S1_B	05:46:07.33	−00:13:43.49	0.320 ± 0.006	0.300 ± 0.008	35.77 ± 19.70	137.32 ± 1.19	89.35 ± 0.51	0.391 ± 0.167	16^{+8}_{-8}	8^{+8}_{-2}	na	na	N	na	na	0	⋯
G205.46-14.56S2	05:46:04.77	−00:14:16.67	0.101 ± 0.014	0.073 ± 0.032	16.83 ± 64.27	24.19 ± 0.25	23.15 ± 0.14	0.069 ± 0.029	46^{+10}_{-10}	42^{+10}_{-10}	na	na	N	381 ± 60	12.5 ± 4.7	1	385
G205.46-14.56S3	05:46:03.63	−00:14:49.57	0.233 ± 0.015	0.194 ± 0.014	130.30 ± 21.59	58.72 ± 1.02	46.67 ± 0.50	0.167 ± 0.072	114^{+8}_{-20}	106^{+8}_{-24}	3.29 ± 2.09	5.03 ± 2.33	Y	178 ± 33	6.4 ± 2.4	1	315
G206.12-15.76	05:42:45.26	−01:16:13.94	0.625 ± 0.013	0.485 ± 0.012	166.34 ± 4.18	363.35 ± 5.66	131.29 ± 1.56	1.035 ± 0.442	22^{+8}_{-8}	26^{+8}_{-8}	1.67 ± 0.06	2.79 ± 1.37	Y	35 ± 9	3.0 ± 1.4	0	400
G206.93-16.61E2_A	05:41:37.19	−02:17:17.34	0.300 ± 0.038	0.228 ± 0.045	156.79 ± 26.01	98.22 ± 4.40	69.25 ± 1.99	0.280 ± 0.120	na	na	na	na	N	198 ± 60	36.0 ± 15.0	111	298
G206.93-16.61E2_B	05:41:37.04	−02:17:17.99	0.206 ± 0.037	0.189 ± 0.045	137.36 ± 76.95	39.17 ± 1.53	31.81 ± 0.76	0.112 ± 0.048	na	na	na	na	N	198 ± 60	36.0 ± 15.0	111	298
G206.93-16.61E2_C	05:41:37.20	−02:17:15.97	1.186 ± 0.148	1.063 ± 0.135	32.30 ± 49.20	76.91 ± 8.68	9.05 ± 0.92	0.219 ± 0.097	na	na	na	na	N	198 ± 60	36.0 ± 15.0	111	298
G206.93-16.61E2_D	05:41:37.15	−02:17:16.52	3.668 ± 0.319	0.720 ± 0.068	76.84 ± 1.35	88.62 ± 7.23	4.90 ± 0.38	0.252 ± 0.110	na	na	na	na	N	198 ± 60	36.0 ± 15.0	111	298
G206.93-16.61W2	05:41:24.93	−02:18:06.75	0.719 ± 0.056	0.508 ± 0.043	99.72 ± 10.31	270.81 ± 17.70	85.08 ± 4.35	0.771 ± 0.333	74^{+22}_{-8}	78^{+22}_{-8}	1.59 ± 0.28	2.68 ± 0.56	Y	31 ± 10	6.3 ± 3.0	0	399
	05:30:51.23	−04:10:35.34	1.011 ± 0.026	0.217 ± 0.013	101.61 ± 0.57	39.69 ± 0.88	14.33 ± 0.24	0.113 ± 0.048	cx	cx	na	na	N	na	na	111	⋯

Table 5
(Continued)

Source	R.A.	Decl.	Maj	Min	PA	$F_{1.3\,mm}$	$Peak_{1.3\,mm}$	Mass	ΔV_B	ΔV_R	Θ_{400}	Θ_{800}	SiO[a] (Y/N)	T_{bol}	L_{bol}	Class[b]	HOPS
	(h:m:s)	(d:m:s)	$''$	$''$	(°)	(mJy)	(mJy/beam)	($M_\odot$)	(km s⁻¹)	(km s⁻¹)	($''$)	($''$)	(N)	(K)	($L_\odot$)		
(1)	(2)	(3)	(4)	(5)	(6)	(7)	(8)	(9)	(10)	(11)	(12)	(13)	(14)	(15)	(16)	(17)	(18)
G207.36-19.82N1_A																111	⋯
G207.36-19.82N1_B	05:30:51.30	−04:10:32.22	0.139 ± 0.035	0.058 ± 0.033	101.42 ± 29.50	3.74 ± 0.10	3.54 ± 0.06	0.011 ± 0.005	na	na	na	na	N	na	na	111	⋯
G208.68-19.20N1	05:35:23.42	−05:01:30.60	0.563 ± 0.015	0.522 ± 0.016	171.29 ± 17.49	811.53 ± 11.28	299.26 ± 3.15	2.312 ± 0.988	na	na	na	na	Y	38 ± 13	36.7 ± 14.5	0	87
G208.68-19.20N2_A	05:35:20.78	−05:00:55.67	14.642 ± 0.458	2.422 ± 0.076	118.87 ± 0.42	212.56 ± 6.58	1.07 ± 0.03	4.777 ± 2.046	na	na	na	na	N	na	na	−1	⋯
G208.68-19.20N2_B[c]	05:35:19.98	−05:01:02.59	0.000 ± 0.000	0.000 ± 0.000	0.00 ± 0.00	3.16 ± 0.23	3.40 ± 0.14	0.009 ± 0.004	na	na	na	na	N	112 ± 10	2.1 ± 1.3	0	89
G208.68-19.20N3_A	05:35:18.06	−05:00:18.19	3.094 ± 0.251	2.073 ± 0.169	149.36 ± 8.06	152.90 ± 12.32	3.95 ± 0.31	0.436 ± 0.189	48^{+12}_{-16}	38^{+12}_{-16}	na	na	Y	na	na	0	⋯
G208.68-19.20N3_B	05:35:18.34	−05:00:32.95	0.224 ± 0.023	0.208 ± 0.031	24.47 ± 62.39	27.24 ± 0.78	21.31 ± 0.38	0.078 ± 0.033	10^{+12}_{-4}	26^{+10}_{-8}	na	na	N	158 ± 20	22.0 ± 8.7	1	92
G208.68-19.20N3_C	05:35:18.27	−05:00:33.93	0.208 ± 0.023	0.181 ± 0.030	173.14 ± 58.56	32.63 ± 0.76	26.59 ± 0.38	0.093 ± 0.040	8^{+10}_{-2}	10^{+8}_{-2}	na	na	N	158 ± 20	22.0 ± 8.7	1	92
G208.68-19.20S_A	05:35:26.56	−05:03:55.11	0.251 ± 0.021	0.124 ± 0.043	169.90 ± 9.26	147.84 ± 3.53	119.82 ± 1.76	0.421 ± 0.180	cx	cx	na	na	N	96 ± 25	49.0 ± 18.0	1	84
G208.68-19.20S_B	05:35:26.54	−05:03:55.71	0.283 ± 0.602	0.255 ± 0.531	40.05 ± 499.81	14.96 ± 20.53	10.41 ± 9.24	0.043 ± 0.061	na	na	na	na	N	96 ± 25	49.0 ± 18.0	1	84
G208.89-20.04E	05:32:48.12	−05:34:41.45	0.183 ± 0.009	0.092 ± 0.014	139.42 ± 5.50	25.80 ± 0.22	23.22 ± 0.12	0.073 ± 0.031	18^{+6}_{-6}	6^{+8}_{-2}	1.72 ± 0.29	2.56 ± 0.42	Y	108 ± 25	2.2 ± 1.0	1	⋯
G208.89-20.04Walma	05:32:28.26	−05:34:19.79	0.340 ± 0.061	0.294 ± 0.065	102.82 ± 89.60	9.77 ± 0.80	6.17 ± 0.34	0.028 ± 0.012	4^{+6}_{-2}	6^{+6}_{-2}	0.62 ± 0.01	0.97 ± 0.19	Y	na	na	0	⋯
G209.29-19.65S1	05:34:55.83	−05:46:04.75	6.581 ± 0.245	2.585 ± 0.096	136.90 ± 1.39	64.14 ± 2.37	0.66 ± 0.02	1.442 ± 0.618	na	na	na	na	N	na	na	−1	⋯
G209.55-19.68N1_A	05:35:08.95	−05:55:54.98	0.376 ± 0.020	0.195 ± 0.029	53.73 ± 5.70	49.57 ± 1.37	32.94 ± 0.59	0.141 ± 0.060	42^{+12}_{-10}	18^{+14}_{-8}	1.28 ± 0.57	1.91 ± 0.86	N	na	na	0	⋯
G209.55-19.68N1_B	05:35:08.63	−05:55:54.65	0.489 ± 0.083	0.352 ± 0.076	120.42 ± 71.17	21.31 ± 2.45	10.59 ± 0.86	0.061 ± 0.027	cx	cx	na	na	N	47 ± 13	9.0 ± 3.7	0	12
G209.55-19.68N1_C	05:35:08.57	−05:55:54.54	1.603 ± 0.085	1.262 ± 0.068	83.11 ± 9.46	46.30 ± 2.36	3.62 ± 0.17	0.132 ± 0.057	na	na	na	na	N	47 ± 13	9.0 ± 3.7	0	12
G209.55-19.68S1	05:35:13.43	−05:57:57.89	0.167 ± 0.013	0.163 ± 0.015	23.17 ± 72.00	92.75 ± 1.13	79.66 ± 0.59	0.264 ± 0.113	24^{+14}_{-8}	38^{+10}_{-8}	1.22 ± 0.21	1.86 ± 0.20	Y	50 ± 15	9.1 ± 3.6	0	11
G209.55-19.68S2	05:35:09.05	−05:58:26.87	0.190 ± 0.012	0.121 ± 0.012	113.66 ± 8.35	29.36 ± 0.40	25.96 ± 0.21	0.084 ± 0.036	22^{+12}_{-8}	28^{+8}_{-6}	1.93 ± 0.76	2.97 ± 0.01	Y	48 ± 11	3.4 ± 1.4	0	10
G210.37-19.53S	05:37:00.43	−06:37:10.90	0.289 ± 0.016	0.216 ± 0.019	152.86 ± 10.12	46.53 ± 0.85	33.66 ± 0.39	0.133 ± 0.057	34^{+8}_{-10}	22^{+14}_{-12}	1.60 ± 0.55	2.41 ± 0.40	Y	39 ± 10	0.6 ± 0.3	0	164
G210.49-19.79W_A	05:36:18.94	−06:45:23.54	0.263 ± 0.015	0.191 ± 0.017	75.98 ± 10.05	70.71 ± 1.16	54.66 ± 0.56	0.201 ± 0.086	38^{+8}_{-8}	36^{+8}_{-8}	2.62 ± 0.85	4.29 ± 0.47	Y	51 ± 20	60.0 ± 24.0	0	168
G210.49-19.79W_B	05:36:18.50	−06:45:23.97	0.435 ± 0.036	0.097 ± 0.060	161.03 ± 5.53	2.77 ± 0.14	1.85 ± 0.06	0.008 ± 0.003	na	na	na	na	N	na	na	111	⋯
G210.82-19.47S_B[c]	05:38:03.43	−06:58:15.89	0.000 ± 0.132	0.000 ± 0.072	0.00 ± 0.00	3.65 ± 0.10	3.53 ± 0.05	0.010 ± 0.004	4^{+4}_{-2}	4^{+4}_{-2}	na	na	N	74 ± 12	0.4 ± 0.2	1	156
G210.97-19.33S2_A	05:38:45.54	−07:01:02.02	0.218 ± 0.025	0.182 ± 0.026	101.22 ± 64.52	7.00 ± 0.21	5.68 ± 0.11	0.020 ± 0.009	10^{+8}_{-4}	14^{+8}_{-4}	1.72 ± 0.13	2.94 ± 1.10	Y	53 ± 15	3.9 ± 1.5	0	377
G210.97-19.33S2_B	05:38:45.02	−07:01:01.68	0.122 ± 0.022	0.107 ± 0.037	20.34 ± 64.74	6.16 ± 0.12	5.70 ± 0.07	0.018 ± 0.008	cx	cx	na	na	N	82 ± 24	4.1 ± 1.6	1	144
G211.01-19.54N	05:37:57.02	−07:06:56.23	0.390 ± 0.005	0.155 ± 0.009	32.90 ± 1.19	45.76 ± 0.35	30.44 ± 0.15	0.130 ± 0.056	14^{+8}_{-6}	12^{+8}_{-6}	1.80 ± 0.58	2.78 ± 0.27	Y	39 ± 12	4.5 ± 1.8	0	153
G211.01-19.54S	05:37:58.75	−07:07:25.72	0.195 ± 0.020	0.153 ± 0.019	102.95 ± 31.20	7.27 ± 0.16	6.19 ± 0.08	0.021 ± 0.009	na	$<20^{+8}_{-8}$	na	na	N	52 ± 8	0.9 ± 0.4	0	152
G211.16-19.33N2	05:39:05.83	−07:10:39.29	0.172 ± 0.027	0.140 ± 0.046	0.94 ± 89.83	5.70 ± 0.16	4.97 ± 0.08	0.016 ± 0.007	8^{+6}_{-2}	10^{+4}_{-2}	na	na	N	70 ± 20	3.7 ± 1.4	0	133
G211.16-19.33N5	05:38:45.33	−07:10:56.03	0.184 ± 0.019	0.088 ± 0.081	31.60 ± 12.06	5.32 ± 0.11	4.71 ± 0.06	0.015 ± 0.006	cx	cx	na	na	N	112 ± 16	1.3 ± 0.5	1	135
G211.47-19.27N_A	05:39:57.33	−07:29:32.73	0.599 ± 0.123	0.210 ± 0.107	133.25 ± 15.03	23.65 ± 3.18	13.04 ± 1.19	0.067 ± 0.030	$<30^{+8}_{-8}$	$<30^{+8}_{-8}$	na	na	N	48 ± 10	1.9 ± 0.8	0	290

Table 5
(Continued)

Source	R.A.	Decl.	Maj	Min	PA	$F_{1.3\ mm}$	Peak$_{1.3\ mm}$	Mass	ΔV_B	ΔV_R	Θ_{400}	Θ_{800}	SiO[a] (Y/N)	T_{bol}	L_{bol}	Class[b]	HOPS
						1.3 mm Continuum (TM1+TM2+ACA)			CO and SiO					Infrared			
	(h:m:s)	(d:m:s)	ʺ	ʺ	(°)	(mJy)	(mJy/beam)	$(M_\odot)$	(km s^{-1})	(km s^{-1})	(ʺ)	(ʺ)		(K)	$(L_\odot)$		
(1)	(2)	(3)	(4)	(5)	(6)	(7)	(8)	(9)	(10)	(11)	(12)	(13)	(14)	(15)	(16)	(17)	(18)
G211.47-19.27N_B	05:39:57.37	−07:29:33.10	0.462 ± 0.227	0.268 ± 0.137	110.05 ± 72.89	13.82 ± 3.15	8.58 ± 1.29	0.039 ± 0.019	$<30^{+8}_{-8}$	$<30^{+8}_{-8}$	na	na	N	48 ± 10	2.1 ± 0.9	0	290
G211.47-19.27S	05:39:56.00	−07:30:27.61	0.616 ± 0.025	0.264 ± 0.026	133.52 ± 3.02	347.68 ± 9.56	180.85 ± 3.44	0.990 ± 0.424	50^{+12}_{-10}	46^{+14}_{-10}	na	na	Y	49 ± 21	180.0 ± 70.0	0	288
G212.10-19.15N1	05:41:21.29	−07:52:27.44	5.813 ± 0.371	3.260 ± 0.210	139.70 ± 4.25	18.26 ± 1.16	0.20 ± 0.01	0.410 ± 0.177	na	na	na	na	N	na	na	−1	⋯
G212.10-19.15N2_A	05:41:23.69	−07:53:46.74	0.193 ± 0.012	0.176 ± 0.010	76.00 ± 74.40	11.84 ± 0.11	10.17 ± 0.06	0.034 ± 0.014	cx	cx	na	na	N	114 ± 10	1.1 ± 0.5	1	263
G212.10-19.15N2_B	05:41:23.99	−07:53:42.22	0.119 ± 0.024	0.044 ± 0.055	19.53 ± 29.51	4.75 ± 0.08	4.54 ± 0.05	0.014 ± 0.006	na	na	na	na	N	160 ± 30	1.1 ± 0.5	1	262
G212.10-19.15S	05:41:26.19	−07:56:51.93	0.251 ± 0.013	0.198 ± 0.020	29.02 ± 11.74	83.33 ± 1.06	66.42 ± 0.52	0.237 ± 0.101	10^{+6}_{-4}	6^{+6}_{-4}	3.90 ± 0.33	6.15 ± 3.30	N	43 ± 12	3.2 ± 1.2	0	247
G212.84-19.45N	05:41:32.07	−08:40:09.77	0.358 ± 0.009	0.278 ± 0.014	171.35 ± 6.91	95.99 ± 1.13	63.47 ± 0.49	0.273 ± 0.117	20^{+6}_{-6}	14^{+6}_{-6}	1.10 ± 0.01	1.82 ± 0.21	N	50 ± 13	3.0 ± 1.2	0	224
G215.87-17.62M_A	05:53:32.52	−10:25:08.18	0.352 ± 0.019	0.222 ± 0.021	55.93 ± 6.79	22.97 ± 0.44	16.35 ± 0.20	0.065 ± 0.028	38^{+12}_{-8}	36^{+10}_{-8}	1.21 ± 0.11	1.46 ± 0.02	Y	na	na	0	⋯
G215.87-17.62N	05:53:42.56	−10:24:00.69	0.164 ± 0.032	0.124 ± 0.038	116.86 ± 44.11	3.30 ± 0.07	2.99 ± 0.04	0.009 ± 0.004	na	na	na	na	N	750 ± 193	82.0 ± 40.0	1	⋯
G215.87-17.62S_off	05:53:25.07	−10:27:30.17	0.147 ± 0.048	0.099 ± 0.043	71.87 ± 89.43	1.21 ± 0.04	1.12 ± 0.02	0.003 ± 0.001	na	na	na	na	N	493 ± 60	0.9 ± 0.5	1	⋯

Notes.

[a] Y = detection and N = for nondetection in SiO.

[b] Starless = −1; Class 0 = 0; Class 1 = 1; Unclassified = 111. The "cx" represents the complex structure; and "na" is not estimated/found.

[c] The objects are likely point sources and they are not resolved in deconvolved 2D Gaussian fitting in combined TM1+TM2+ACA beams. Further investigation is required to confirm their candidacy.

(This table is available in machine-readable form.)
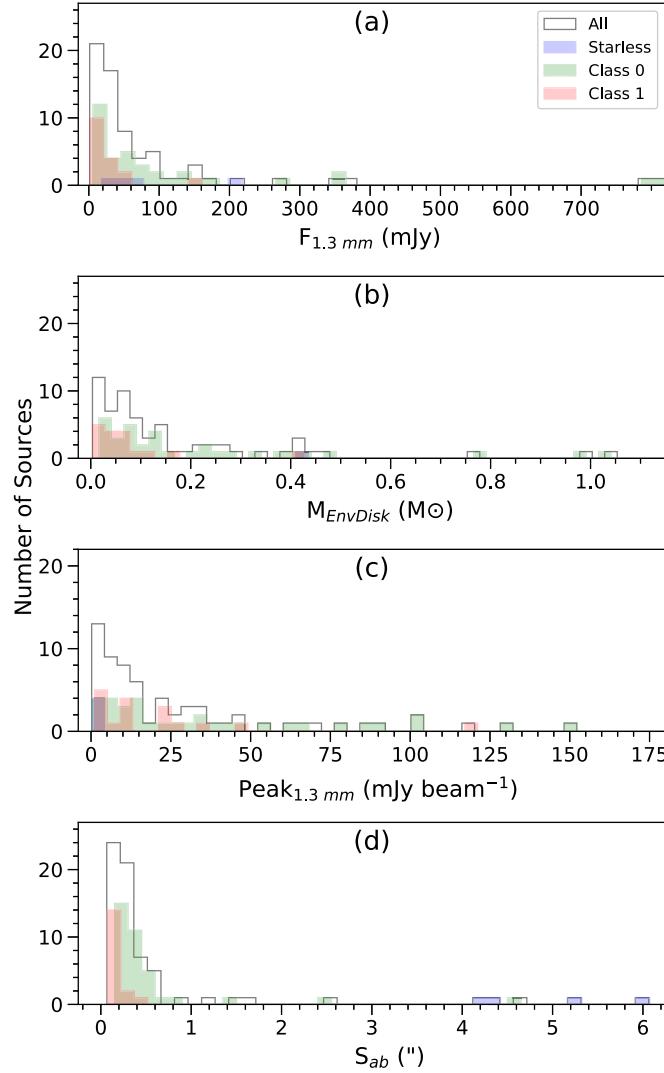
Figure 4. Histograms of (a) integrated flux densities, (b) envelope+disk mass, (c) peak emission, and (d) geometrical sizes derived with 2D Gaussian fitting of 1.3 mm continuum emission for all the sources (black steps), including starless (blue), Class 0 (green), Class I (red), and unclassified sources.

Figure 5. Example of molecular outflow detected at ALMA ^{12}CO(2–1) (gray) is shown for a Class I source G205.46-14.56S3. Black contours are at $3n\sigma$, where $n = 1, 2, \ldots$ and $\sigma = 0.14$ Jy/beam km s^{-1}. Blue and red arrows indicate the blueshifted and redshifted emissions, respectively. Magenta contours are 1.3 mm continuum emission at levels $6 \times (1, 3, 8, 16)\sigma$, where $\sigma = 6 \times 10^{-5}$ Jy beam^{-1}. Blue and red contours are blue- and redshifted integrated SiO(5–4) emission at $3 \times (1, 2, 3, 6, 9)\sigma$, where $\sigma = 0.03$ Jy beam^{-1}. Average tangents through the 3σ outermost contours at $\sim 1''$ and $\sim 2''$ from the continuum peak are drawn in cyan dashed lines. Yellow and green double-headed arrows indicate the opening angle width $[\Theta_{\rm obs}]_{400}$ and $[\Theta_{\rm obs}]_{800}$, respectively, which are at different distance of $\sim 1''$ and $\sim 2''$ from the continuum peak, respectively. A schematic of opening angle (α) measurement is also shown (see text for details).
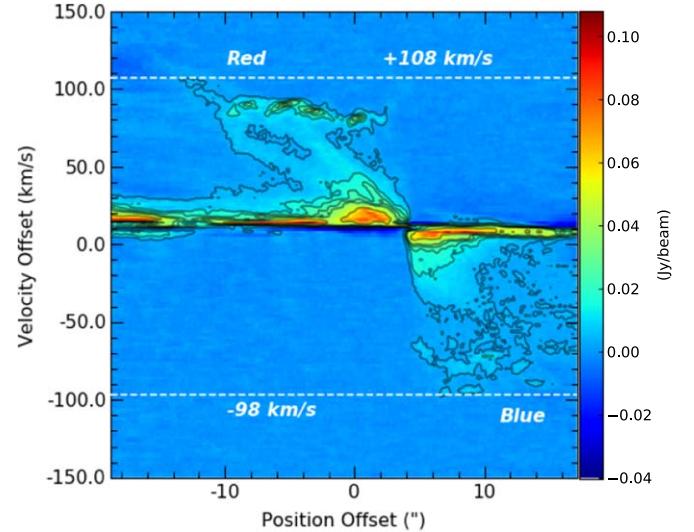
Figure 6. Position–velocity diagram of ^{12}CO molecular outflow emission along jet axis for G205.46-14.56S3. Black contour levels are at $3 \times (1, 2, 3, 4, 6, 10, 15)\sigma$, where $\sigma = 0.001$ Jy beam^{-1}. Systemic velocity of the source is $\sim +12 \pm 4$ km s^{-1}. Prominent nearly continuous emission can be seen up to -98 and $+108$ km s^{-1} in the blue- and redshifted lobes, respectively. Including the near-source overlapping blue- and redshifted emission, the velocity extents are obtained as $\Delta V_B \sim 114$ km s^{-1} and $\Delta V_R \sim 106$ km s^{-1} for blue- and redshifted lobes, respectively.

The distribution of $T_{\rm bol}$ can be seen in Figures 7(a) and (b) (see also Figures 9 and 10). Figure 7(c) shows the distribution of $L_{\rm bol}$ with the $T_{\rm bol}$ of our protostellar sample. Two separate wings are prominent in Figure 7(c), where the nearly horizontal wing represents the increment from Class 0 to Class I sources. The nearly vertical wing possibly originates from the combined luminosity of multiple stellar components, since they possess a common envelope and the present available infrared resolution is not enough to distinguish their emission components. We estimated the bolometric temperature of 53 sources—those having five or more wavelength detections—which also includes all sources in multiple systems.

3.3.2. Outflows in Protostellar Candidates

The detection of infrared emission could be biased by the high background emission from the ambient cloud. In addition, Herschel does not have coverage of all the Orion dense cores. Hence, some of the protostars in this ALMASOP sample could not be detected from the infrared-only catalog. Outflows are

another potential tool to identify protostars. As such, eight sources (G192.32-11.88N, G205.46-14.56M1_B, G205.46-14.56S1_B, G208.68-19.20N3_A, G208.89-20.04W, G209.55-19.68N1_A, G211.47-19.27N_B, G215.87-17.62M_A) are not listed in the infrared catalog, but they do have bipolar CO
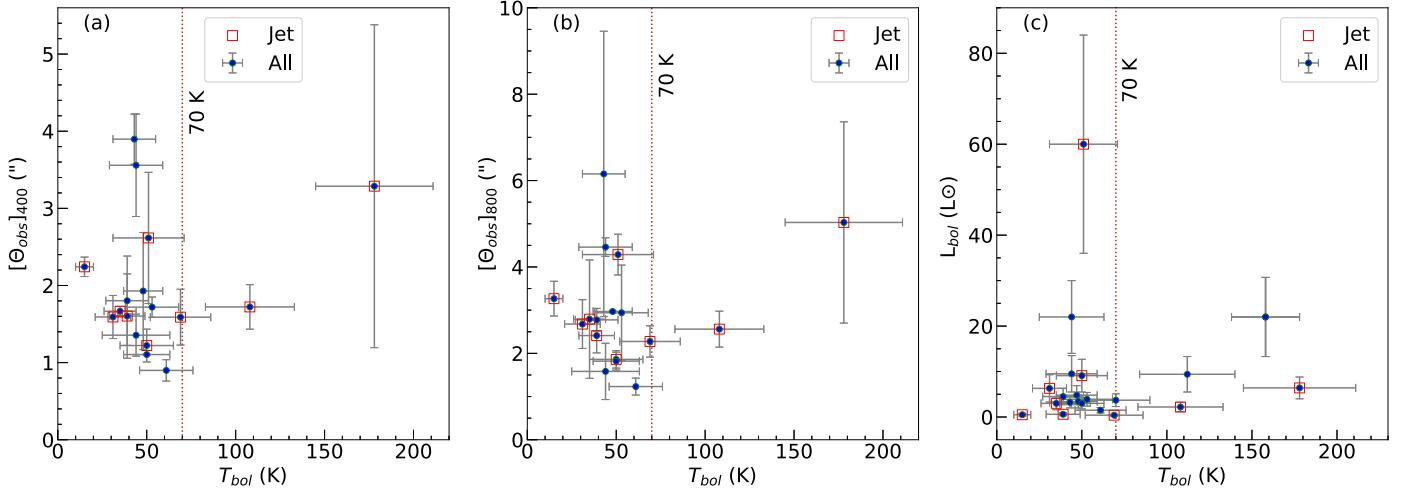
Figure 7. Opening angle Θ_{op} ($''$), i.e., the average width of the blue- and redshifted outflow cavity (a) at $\sim$400 au and (b) at $\sim$800 au from continuum peak, as a function of T_{bol} (K) for the protostars of the survey sample. Panel (c) shows $L_{bol}(L_\odot)$ as function of T_{bol} (K). Blue data points with gray error bars represent all the outflow sources having a good detection in both blue- and redshifted outflow lobes. Red squares indicate the sources with SiO knot detection (i.e., jet emission). Dotted vertical lines in all three panels are indicating $T_{bol} = 70$ K, a boundary between Class 0 to Class I sources (see text for details).

outflows. We consider these sources to be likely young Class 0 sources. However, the complex cloud dynamics prevent the detection of less extended and evolved outflows in CO (2–1), which are marked as "cx" in Table 5.

Finally, we classify 56 sources based on T_{bol} estimation and outflow detection. Out of them, 19 are candidate Class I sources, and the other 37 sources are candidate Class 0 sources. However, higher-resolution multiband infrared observations would more effectively refine the classification. For some sources in multiple systems (e.g., G196.92-10.37_C, G205.46-14.56M2_A, and G206.93-16.61E2_A - D), we obtain T_{bol}, but there are no clear signatures of outflows. The infrared emission for those sources are also easily confused with others. These sources are not classified in this paper.

3.4. Candidates for Class 0 Keplerian-like Disks

The ALMASOP project also aims to search for Keplerian-like disks surrounding Class 0 protostars. Figure 11 presents a candidate Keplerian-like disk surrounding a Class 0 protostar, G192.12-11.10. Its ^{12}CO $J = 2$–1 emission reveals a collimated bipolar outflow (see left panel of Figure 11). As shown in the right panel of Figure 11, the 1.3 mm continuum emission of G192.12-11.10 shows a flattened structure that may be a candidate disk. The redshifted and blueshifted $C^{18}O$ $J = 2$–1 emission clearly shows a rotation pattern of the disk-like structure. We have identified a handful of disk candidates surrounding Class 0 protostars such as G192.12-11.10. The properties of these disk candidates will be discussed in a forthcoming paper (S. Dutta et al. 2020, in preparation).

3.5. Chemical Signatures

As illustrated in Table 3, the four SPWSs cover a suite of molecular species and transitions, most of which are of importance for the chemical diagnostics of young star-forming regions. The successful detection and imaging of these tracers enables the analysis of chemical compositions of our diverse sample of objects from starless to young Class 0 and Class I protostellar cores.

It has been suggested that the deuterium fraction increases at the cold starless core phase and then decreases as the protostar warms up the surrounding material in the protostellar phase (e.g., Tobin et al. 2019; Tatematsu et al. 2020). As shown in Figures 12 and 13, N_2D^+ and DCO^+ are detected toward both starless and protostellar cores. The emission morphology will aid in diagnosing their thermal structure and history, which will be discussed in forthcoming papers (D. Sahu et al. 2020, in preparation; S.-Y. Liu et al. 2020, in preparation).

Some low- to intermediate-mass Class 0/I protostars, dubbed "hot corinos," exhibit considerably abundant saturated complex organic molecules (COMs: CH_3OH, H_2CO, $HCOOCH_3$, HCOOH) in the compact (<100 au) and warm ($\sim$100 K) regions immediately surrounding the YSO (e.g., Ceccarelli 2004; Kuan et al. 2004), as shown in Figure 14. By utilizing our ACA 7 m data, Hsu et al. (2020) have readily identified four new hot corino candidates (G192.12-11.10, G211.47-19.27S, G208.68-19.20N1, and G210.49-19.79W) in the sample. A more detailed study of hot corinos with high-resolution 12 m array data will be presented in a forthcoming paper (S.-Y. Hsu et al. in preparation).

As discussed in Section 3.2.1 and 3.2.2, the outflow and jet components and their interaction with the core can be traced both in position and velocity by ^{12}CO and SiO line emission. The other molecular species such as CS, $C^{18}O$, CH_3OH, C_3H_2, OCS, HCO^+ could be utilized to trace the dense structures underlying protostellar winds (e.g., Jørgensen et al. 2004; Codella et al. 2005; Maret et al. 2005; Arce et al. 2007; Lee 2020). The molecular species available in observed spectra are displayed in Figures 13 and 14. The shock chemistry with ALMASOP data will be presented in a forthcoming paper (S.-Y. Liu et al. 2020, in preparation).

4. Discussion

4.1. Evolution of the Dense Cores

From the 1.3 mm continuum morphology of the 70 dense cores and their infrared counterpart, we perceived three categories. The first category consists of 48 dense cores that are relatively compact in 1.3 mm continuum with protostellar

Figure 8. Maximum outflow velocity (ΔV) for (a) blueshifted, (b) redshifted, and (c) average of both velocity components as a function of $[\Theta_{obs}]_{400}$ ($''$). Symbols are same as for Figure 7. Linear regression is shown with a brown line in panel (c).

complex cloud dynamics and confusing infrared detection. Moreover, out of 72 targeted JCMT positions, 24 show no emission in the combined TM1+TM2+ACA continuum maps. They are likely the starless cores with low density and with sizes larger than the maximum recoverable size, as discussed above (see Section 3.1 and Figure 3). However, 10 out of the 24 starless cores are detected with ACA alone. The detailed properties of all the starless cores will be presented in a forthcoming paper (D. Sahu et al. 2020, in preparation).

Figure 4(a)–(d) shows the histogram distribution of all types of sources, which includes starless, Class 0, Class I, and unclassified sources. The starless, Class 0, and Class I have median values of $F_{1.3\,mm} \sim 59.65$, 46.42, and 14.96 mJy, respectively, whereas the median values of $M_{EnvDisk}$ are 1.34, 0.13, 0.04 $M_{\odot}$, respectively. A similar sequence was observed at 4.1 cm and 6.1 cm fluxes in Tychoniec et al. (2018), where Class 0 sources exhibit larger flux than Class I in both wavelengths. The geometrical sizes, S_{ab}, of the starless cores (deconvolved median size $\sim 4''.77$) are found to be larger than Class 0 (median deconvolved size $\sim 0''.32$) and Class I (median deconvolved size $\sim 0''.18$). The Gaussian 2D integrated flux and sizes of the dense cores basically depend on the power-law indices, which vary from starless to Classes 0 and I (e.g., Lee et al. 2019). Thus, the above outcomes could be interpreted as varying density profiles (e.g., Aso et al. 2019). The starless cores have a flat density distribution in the inner regions, so we get larger sizes and hence larger masses. On the other hand, the small sizes from Class 0 to Class I sources suggest that pseudodisk/disks are dominating the 1.3 mm fluxes and the apparent mass-supplying radius of the continuum reduces with the evolution from Class 0 to Class I (see also Figure 10(c), Section 4.2). These decreasing sizes and masses findings from Class 0 to Class I could also indicate the dissipation of the envelope due to accretion and ejection activity of the protostars from Class 0 to Class I evolution. However, our present analyses of one-component 2D-Gaussian fitting could not infer to the presence of secondary sources within the common envelope. Therefore, the actual envelope size of the individual sources could not be specified; in those cases, 2D-Gaussian fittings with two or more components are required. It is also not clear from only our present sample (which consists of a small fraction of Class I sources) whether these are the intrinsic correlations of dense core evolution or are biased by the sample selection; more statistical studies may explain this more comprehensively.

Likewise, if we compare the Peak$_{1.3\,mm}$, the Class 0 sources have larger values of peak emission (median ~ 28.20 mJy beam^{-1}) than Class I (median ~ 10.41 mJy beam^{-1}) and starless cores (median ~ 0.52 mJy beam^{-1}). This result suggests a possible evolutionary trend of the dense cores whereby the starless cores exhibit a lower peak, and as they form a Class 0 system, their emission heats up the surrounding disk-envelope material, making them brightest in this wavelength. On the other hand, as they evolve to a Class I system, their surrounding material may also dissipate and the stellar core may become more luminous toward the shorter wavelength regime, hence they tend to show a fainter peak in the 1.3 mm wavelength. However, this could be also an interferometric effect; as starless cores are more diffuse, the emission is resolved out. Protostellar cores are denser with a different density profile, which can be recovered by the interferometer because they are compact.

Figures 10(a) and (b) displays the distribution of 1.3 mm flux densities and peak flux, respectively, as a function of T_{bol}. The Class I (i.e., $T_{bol} > 70$ K) sources are mostly concentrated at

signatures, as well as either low-velocity outflow, high-velocity jet, or infrared detections. In the second category, four dense starless cores exhibit extended emission and compact blobs (see Table 5). They are likely prestellar cores with substructures, and deserve detailed investigation. The physical and chemical properties of these four cores will be further discussed in forthcoming papers (D. Sahu et al. 2020, in preparation; N. Hirano et al. 2020, in preparation). In the third category, another 16 dense cores remain unclassified due to their

Table 6
SED Data for the Continuum Peak

Source	⋯	K_{2mass} [2.159]	eK_{2mass}	⋯	Wise1 [3.4]	eWise1	⋯	pacs1 [70]	epacs1	⋯	akari09 [09]	e_akari09	⋯	JCMT850 [850]	eJCMT850	⋯	IRAC1 [3.6]	eIRAC1	⋯
G196.92-10.37_C	⋯	7.310e−03	8.156e−07	⋯	1.845e−02	4.606e−04	⋯	⋯	⋯	⋯	1.972e−01	3.200e−02	⋯	5.145e+00	4.991e+00	⋯	⋯	⋯	⋯
G200.34-10.97N	⋯	8.589e−04	8.834e−08	⋯	9.744e−04	2.962e−05	⋯	⋯	⋯	⋯	⋯	⋯	⋯	6.507e−01	6.349e−01	⋯	⋯	⋯	⋯
G201.52-11.08	⋯	2.910e−03	4.078e−07	⋯	4.047e−03	1.011e−04	⋯	⋯	⋯	⋯	⋯	⋯	⋯	1.095e−01	2.032e−02	⋯	⋯	⋯	⋯
G203.21-11.20W1	⋯	⋯	⋯	⋯	1.630e−05	6.532e−06	⋯	⋯	⋯	⋯	⋯	⋯	⋯	1.538e+00	1.772e−01	⋯	⋯	⋯	⋯
G203.21-11.20W2	⋯	⋯	⋯	⋯	1.463e−04	1.112e−05	⋯	⋯	⋯	⋯	⋯	⋯	⋯	1.374e+00	1.308e−01	⋯	⋯	⋯	⋯
G205.46- 14.56M1_B	⋯	⋯	⋯	⋯	⋯	⋯	⋯	⋯	⋯	⋯	⋯	⋯	⋯	3.908e+00	2.886e−01	⋯	⋯	⋯	⋯
G205.46-14.56M1_A	⋯	⋯	⋯	⋯	2.344e−03	6.616e−05	⋯	6.050e+00	3.038e−01	⋯	⋯	⋯	⋯	3.908e+00	2.886e−01	⋯	3.339e−03	1.680e−04	⋯
G205.46-14.56M2_A	⋯	1.114e−02	7.392e−06	⋯	5.769e−02	2.819e−03	⋯	8.588e+00	8.588e−01	⋯	⋯	⋯	⋯	1.123e+00	1.315e−01	⋯	3.007e−02	1.507e−03	⋯
G205.46-14.56M2_B	⋯	1.114e−02	7.392e−06	⋯	5.769e−02	2.819e−03	⋯	8.588e+00	8.588e−01	⋯	⋯	⋯	⋯	1.123e+00	1.315e−01	⋯	3.007e−02	1.507e−03	⋯
G205.46-14.56M2_C	⋯	2.284e−02	7.380e−06	⋯	1.350e−01	3.225e−03	⋯	2.455e+01	2.455e+00	⋯	1.432e+00	7.350e−03	⋯	3.022e−01	4.168e−02	⋯	1.620e−01	8.115e−03	⋯
G205.46-14.56M2_D	⋯	2.284e−02	7.380e−06	⋯	1.350e−01	3.225e−03	⋯	2.455e+01	2.455e+00	⋯	1.432e+00	7.350e−03	⋯	3.022e−01	4.168e−02	⋯	1.620e−01	8.115e−03	⋯
G205.46-14.56M2_E	⋯	⋯	⋯	⋯	⋯	⋯	⋯	⋯	⋯	⋯	⋯	⋯	⋯	3.022e−01	4.168e−02	⋯	⋯	⋯	⋯
G205.46-14.56M3	⋯	⋯	⋯	⋯	⋯	⋯	⋯	⋯	⋯	⋯	⋯	⋯	⋯	2.477e−01	3.847e−02	⋯	⋯	⋯	⋯
G205.46-14.56N1	⋯	⋯	⋯	⋯	⋯	⋯	⋯	4.137e−01	2.102e−02	⋯	⋯	⋯	⋯	6.534e−01	7.695e−02	⋯	5.672e−06	⋯	⋯
G205.46-14.56N2	⋯	⋯	⋯	⋯	⋯	⋯	⋯	6.514e−01	3.293e−02	⋯	⋯	⋯	⋯	3.022e−01	4.168e−02	⋯	7.795e−06	⋯	⋯
G205.46-14.56S1_A	⋯	⋯	⋯	⋯	2.591e−03	9.003e−05	⋯	6.220e+01	3.113e+00	⋯	⋯	⋯	⋯	7.140e+00	6.893e−01	⋯	⋯	⋯	⋯
G205.46-14.56S1_B	⋯	⋯	⋯	⋯	⋯	⋯	⋯	⋯	⋯	⋯	⋯	⋯	⋯	7.140e+00	6.893e−01	⋯	⋯	⋯	⋯

Notes. This table contains all the cross-matching fluxes. Here, T_{bol} and L_{bol} are estimated with the fluxes having good photometric accuracy (see text for details).

(This table is available in its entirety in machine-readable form.)
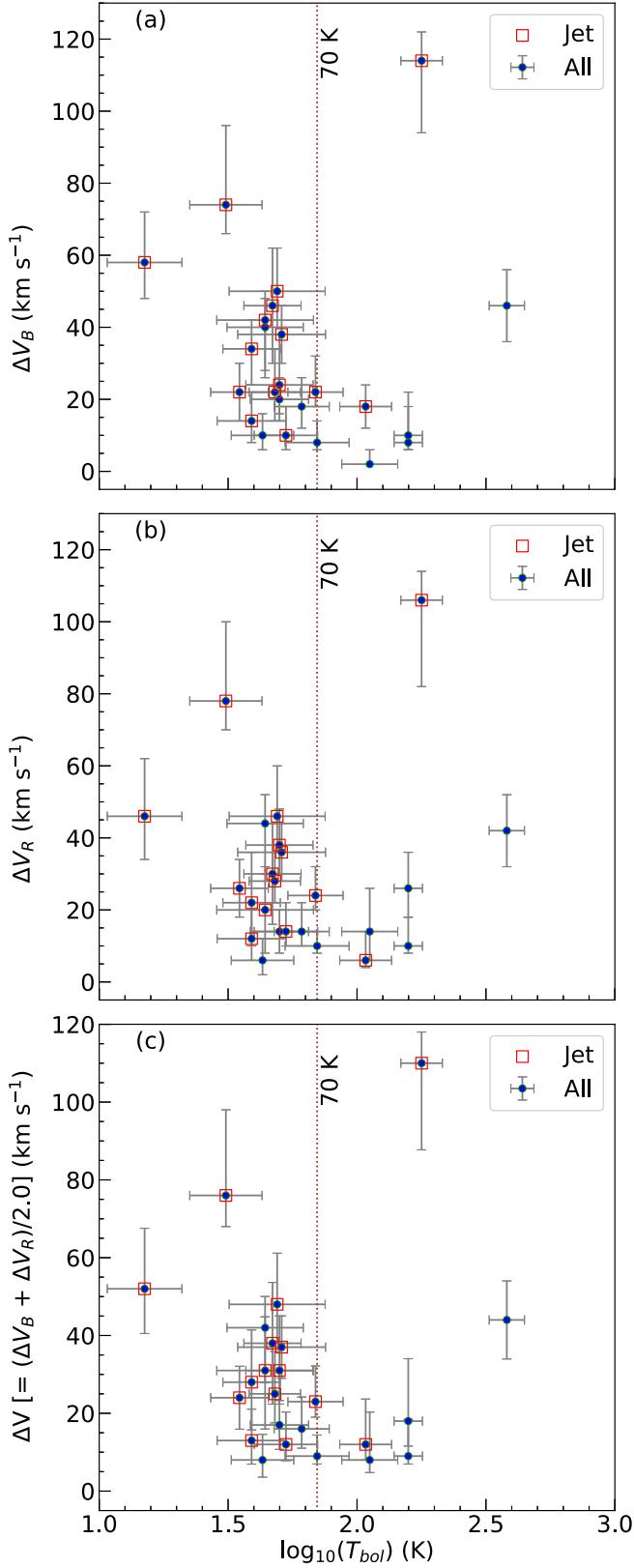
Figure 9. Maximum outflow velocity (ΔV) for (a) blueshifted, (b) redshifted, and (c) average of both velocity components as a function of T_{bol}. Symbols are same as Figure 7. The majority of the Class 0 sources (i.e., $T_{bol} < 70$ K) follow an increasing trend in all three panels.

$\log(F_{1.3\,\mathrm{mm}}) \sim 1.3$–$1.8$ mJy and $\log(\mathrm{Peak}_{1.3\,\mathrm{mm}}) \sim 1.25$–$1.70$ mJy beam^{-1}, whereas the Class 0 flux densities and peaks are widespread. Figure 10(c) shows the decreasing size distribution of

2D Gaussian fitting with T_{bol}. Although a small number of Class I sources are available in this sample, and the disk-scale geometry of the sources are not properly resolved with the present spatial resolution (~140 au), these Class I sources are found to have significantly smaller sizes than Class 0. Figure 10(c) points toward a transition from Class 0 to Class I at $T_{\mathrm{bol}} = 60$–70 K for envelope +disk size $<0''2$ (i.e., 80 au) in this sample, which is also an empirical boundary temperature between Class 0 to Class I sources. These findings also support either possible density variation according to a power-law index, or that envelope dissipation with protostellar evolution could contribute toward such flux, peak, and size variation from Class 0 to Class I.

4.2. Evolution of Protostellar Outflows

The bolometric temperature and luminosity derived from SED analyses can be somewhat questionable due to inconsistent multiwavelength data catalogs and misidentification due to multiplicity. Rather than exclusively depending on the SED results, we also searched for the possible evolutionary trends of the protostars from the physical appearance of the outflows such as outflow opening angle, and maximum outflow velocity in the ISM.

4.2.1. Time Sequence Outflow Opening Angle

Protostellar jets and winds propagate into the envelope as its immediate environment. As the protostars evolve, the collapsing material settles into the equatorial pseudodisk along with the magnetic field lines. As the pseudodisk grows in size, the matter is evacuated by the magnetic field from the polar region. It is to be noted that the envelope mass declines typically a few orders of magnitudes during the evolution from Class 0 to Class I (Bontemps et al. 1996; Arce & Sargent 2006). The excavated surroundings set off the widening opening of the wind-blown outflow lobe with time (e.g., Bachiller & Tafalla 1999; Arce & Sargent 2006; Shang et al. 2006).

The outflow opening angle remains narrower than 20° independent of the launching protostar's properties (e.g., mass of the protostars, ejection to accretion mass ratio) during the early stages (Kuiper et al. 2016), and the low-velocity outflow appears from the first core (Larson 1969), without any high-velocity component. The high-velocity jet catches up to the outflow after a few hundred years, and the jet speed increases with time (e.g., Machida & Basu 2019). The emergence of the jet pushes the outflow material outward (Kuiper et al. 2016; Machida & Basu 2019). The observed opening angles are observed to span over 20° in early accretion phases and up to 160° at later phases (Beuther & Shepherd 2005; Frank et al. 2014). For example, HH 211 is among the youngest known Class 0 protostars with narrow opening angle (Bachiller & Tafalla 1999), while the evolved Class 0 or embedded Class I systems (e.g., HH 46/47; van Kempen et al. 2009) have relatively wider opening angles of their outflow cavity (van Kempen et al. 2009). The older outflow cavities driven by Class I sources, such as L 43, L 1551, and B5 (Richer et al. 2000), appear characteristically with low-velocity CO outflows from wider opening cavities up to 90° (Lee et al. 2002; Arce & Sargent 2006). Observations of a large number of outflows at different evolutionary stages from Class 0 and Class I to Class II, revealed a systematic widening of opening angle with the stellar evolution (Arce & Sargent 2006; Velusamy et al. 2014; Hsieh et al. 2017).
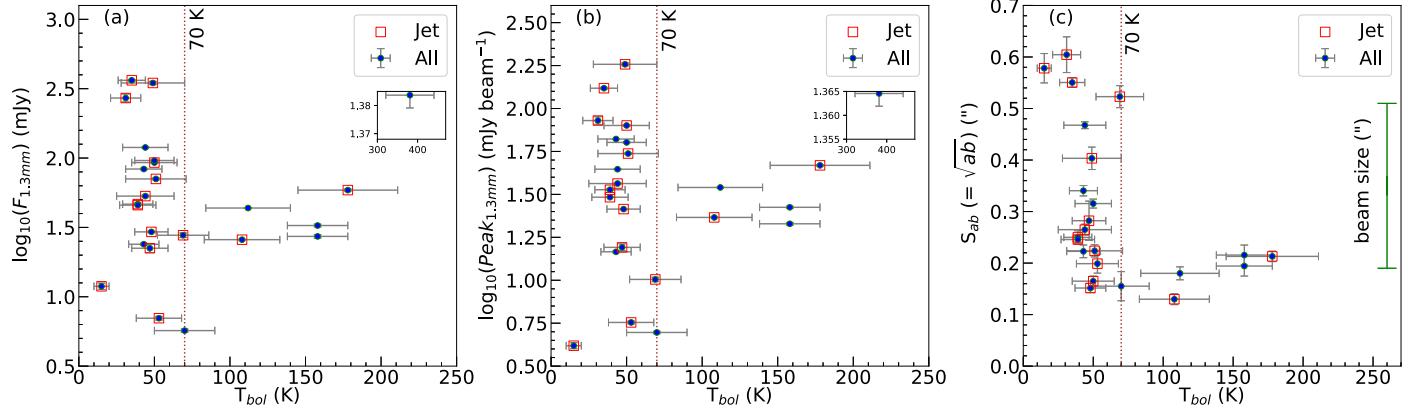
Figure 10. (a) Flux densities, (b) peak, (c) deconvolved size at 1.3 mm from 2D Gaussian fitting as a function of T_{bol}. Symbols are same as for Figure 7. The y-axis error bars are shown at inset figures in panels (a) and (b). Typical beam size is shown in panel (c).
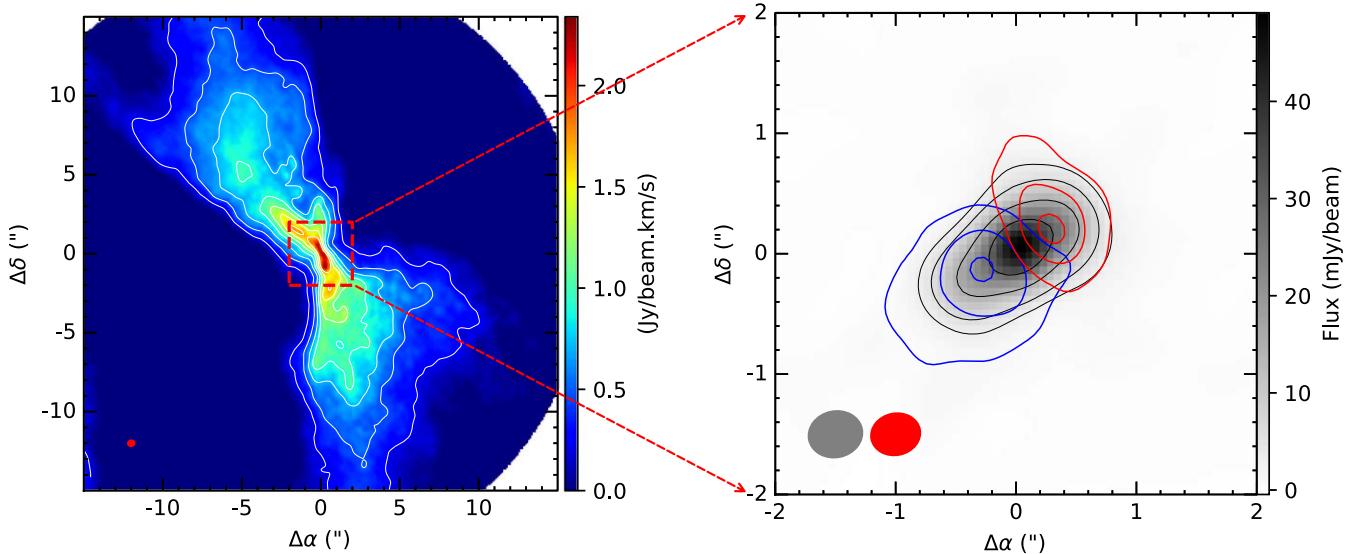
Figure 11. Left panel displays ALMA $^{12}CO(2-1)$ integrated intensity (moment zero) color-scale map of the source G192.12-11.10. White contours start from 10% to 70% in steps of 10% of the intensity peak. CO intensity peak is 2.3 Jy beam^{-1} km s^{-1}. Synthesized beam size is shown in the bottom left corner in red. Right panel presents a zoomed-in view of the central part. Blueshifted (blue contours) and redshifted (red contours) components of $C^{18}O(2-1)$ emission are overplotted on top of 1.3 mm continuum images. Blue and red contours are at 10, 20, 30σ, where the noise level is $\sigma \sim 0.017$ Jy beam^{-1} km s^{-1}. Gray scale is the 1.3 mm continuum emission with contour levels at $(n^2+1) \times 50\sigma$, with $\sigma = 0.06$ mJy beam^{-1}. Synthesized beam sizes are shown in the bottom left corner in gray (continuum) and red ($C^{18}O$).

In Figure 7(a) and (b), the opening angles are plotted as a function of the T_{bol}. The Class I sources exhibit a higher opening angle range (median $[\Theta_{obs}]_{400} \sim 2\farcs7$) than Class 0 ($[\Theta_{obs}]_{400} \sim 1\farcs6$). However, from the present scattered distribution, a linear regression suggests a minor correlation only, which may be due to a limited number of opening angle measurements at >70 K (i.e., only three in Class I and none in Class II), high uncertainty in T_{bol} estimation, and/or unknown inclination of the outflow axis. Additional observations of more Class I and early Class II are required in order to obtain the evolutionary changes of opening angle accurately, as observed in Arce & Sargent (2006), Velusamy et al. (2014), Hsieh et al. (2017).

4.2.2. Age Dispersal Velocity Distribution

Several outflow models have been proposed to demonstrate the formation of molecular outflow driven by protostars and how they propagate in the ambient cloud environment; for details, see the reviews by Arce et al. (2007) and Frank et al. (2014). The two more broadly accepted models are: (a) the disk-wind model (e.g., Konigl & Pudritz 2000), where a wind-driven outflow is launched from the entire protostellar disk surface; and (b) a two-component protostellar wind model or X-wind model (e.g., Shu et al. 2000), initiated from the innermost region of the disk. In the X-wind model, the disk wind could drive a slow wide-angle outflow along with a collimated central fast-moving jet component. This model also predicts that the wide-opening angle near an outflow-launching protostar could escalate a large radial velocity extent (Pyo et al. 2006; Hartigan & Hillenbrand 2009). One potential interesting constraint from Figure 5 is that a fraction of blueshifted emission occurs on the redshifted side—and similarly, a fraction of redshifted emission occurs on the blueshifted side. This could be explained either by the wider line width produced by disk wind (Shang et al. 1998; Pesenti et al. 2004; Liu & Shang 2012) or the inclination angle of the outflow axis.
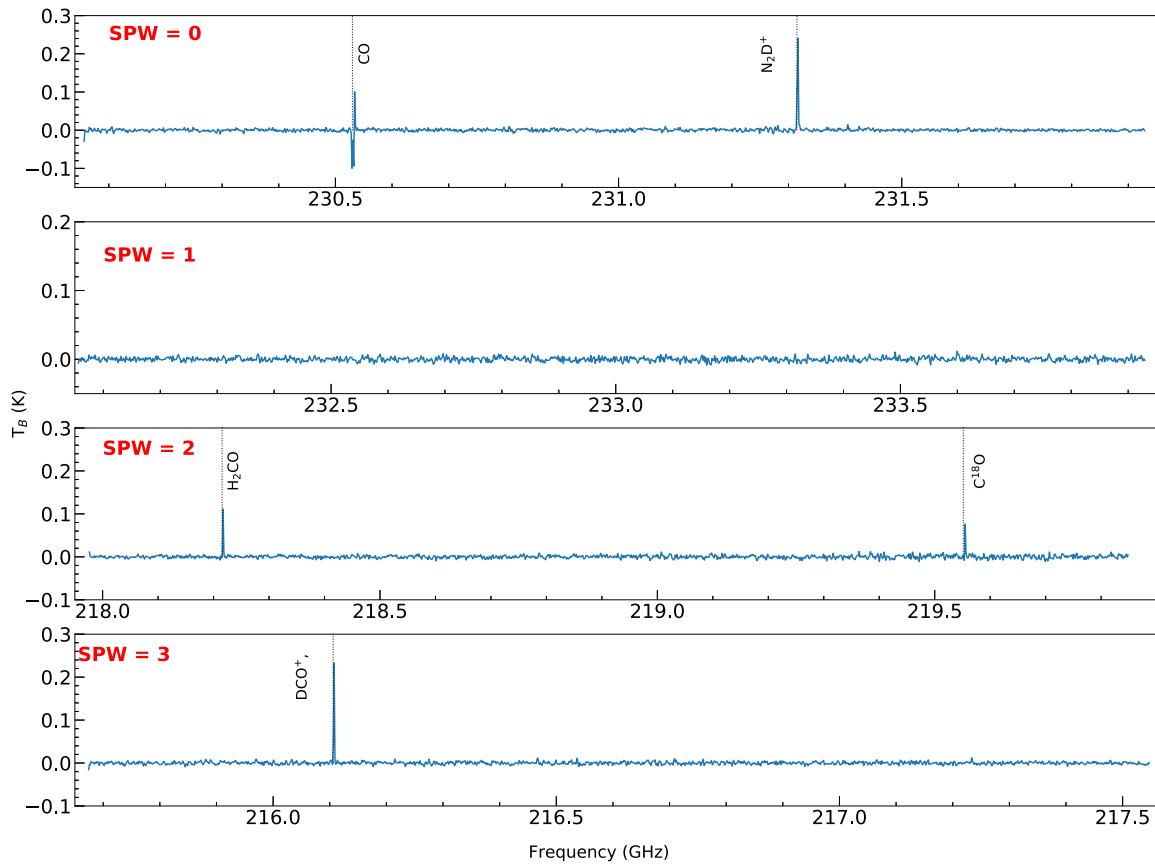
Figure 12. Spectra of the starless dense core G209.29-9.65S1 in four spectral windows (SPWS; see Table 3) observed in combined TM1+TM2 + 7m-ACA configurations. Various identified lines are marked.

We can infer something about the flow plateau with the velocity extent, assuming that all the outflow wings provide consistent measurements for equal FOV (see also Section 3.2.1). The outflow velocity $V_{real} = V_{obs}/\cos(i)$, where V_{obs} is the observed radial velocity. The velocity extent of the outflow caused by the observed opening angle (Θ_{obs}), $\Delta V = V_{real}\sin(i)\Theta_{obs}$; implying $\Delta V = V_{obs}\tan(i)\Theta_{obs}$, where $\Theta_{obs} = \Theta_{real}\sin(i)$. Thus, to establish a correlation between ΔV and Θ_{obs}, we need a reliable estimation of inclination angle, which we are lacking. Moreover, if we assume a random distribution of inclination angles, the mean value is given by $\bar{i} = \int_0^{\pi/2} i\sin(i)di = 1\,\text{rad} = 57^\circ\!.3$, which will lead to homogeneous projection effects. Therefore, we adhere to the observed value of velocity extent and Θ_{obs} to search for a correlation.

Figure 8 shows that the value of ΔV_{obs} increases with Θ_{obs}. A linear regression provides:

$$\Delta V_{obs} = 25.45(\pm 6.55)\,[\Theta_{obs}]_{400} - 10.45(\pm 11.63).$$

This can be explained by considering the opening angle as an indicator of age (see also Section 4.2.1). In the early stages of the protostars, the outflow is detected in small velocity ranges around the systemic velocity. With protostellar evolution, the central mass of the protostars keeps growing, and then higher-energy outflows/ jets are likely to originate from a deeper gravitational potential well, thus one can expect a higher ΔV_{obs}. In Figure 8, two non-jet sources, G192.12-11.10 and G212.10-19.15S, exhibit smaller ΔV_{obs} with higher Θ_{obs}; these may be evolved Class 0 sources ejecting weak disk winds. However, they deserve to be probed via

evolved outflow tracers as well as more high-density jet tracers like higher transitions of SiO.

Such a correlation could be largely due to the unknown inclination angle of the observable parameters. In the absence of proper inclination measurements, we have applied the major-to-minor axis aspect ratio of the 1.3 mm continuum emission as a proxy to the inclination correction, and the above correlation is found to be more scattered—although the overall increasing trend remains the same. However, this aspect ratio could also show larger values for geometrically thick disk-envelope systems (e.g., Lee et al. 2018).

In Figure 9, the ΔV_{obs}s for Class 0 sources are found to be distributed from 4 to 110 km s^{-1}, whereas evolved Class I sources show mostly toward smaller CO ΔV_{obs}. Additionally, all jet sources have higher values of ΔV_{obs} (median $\sim$24 km s^{-1}) than the non-jet sources (median $\sim$16 km s^{-1}), suggesting more active accretion and a higher mass-loss rate of jet sources in comparison to nonjet sources. One exception occurs for the source G208.89-20.04E, which is located in a complex cloud environment and also has overlapping blue- and redshifted velocity channels, possibly indicating a high inclination angle to the line of sight.

In summary, as the protostar evolves, the outflow cavity opening widens and the protostar ejects more energetic outflowing material, as expected if outflow originates from the deeper gravitational potential well of an evolved protostellar.

5. Summary and Conclusion

We have conducted a survey toward 72 dense cores in the Orion A, B, and λ Orionis molecular clouds with ALMA
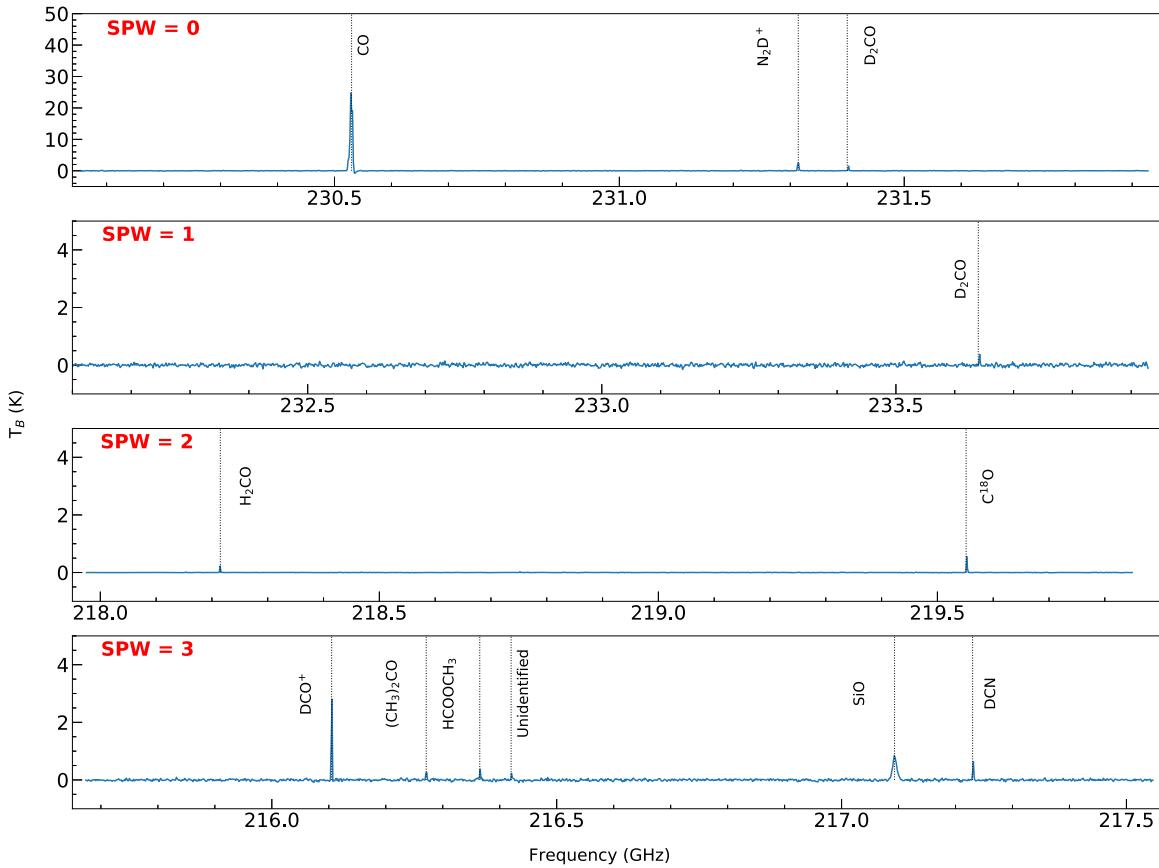
Figure 13. Spectra of the protostellar object G191.90-11.21S. All SPWs, array configurations, and line identifications are same as Figure 12.

1.3 mm continuum in three different resolutions (TM1 $\sim 0''\!.35$, TM2 $\sim 1''\!.0$, and ACA $\sim 7''\!.0$). This unique combined configuration survey enables us to characterize the dense cores at unprecedentedly high sensitivity at this high resolution. The main outcomes are as follows:

1. We are able to detect emission in 44 protostellar cores and four candidate prestellar cores in the combined three configurations, where another 10 starless cores have detection in the individual ACA array configurations. The starless, Class 0, and Class I sources have continuum median deconvolved sizes of $\sim 4''\!.77$, $0''\!.32$, and $0''\!.18$, respectively, decreasing with dense core evolution. The peak emission of Class 0, Class I, and starless cores are 28.20, 10.41, 0.52 mJy beam^{-1}, respectively, suggesting that, with protostellar formation, the envelope is heated up in Class 0 and the envelope loses material while transitioning from Class 0 to Class I.

2. A total of 37 sources show CO outflow emission, and 18 ($\sim$50%) of them also show high-velocity jets in SiO. The CO velocity extends from 4 to 110 km s^{-1}, with a median velocity of 26.5 km s^{-1}. The CO outflow cavities have opening angle widths at $1''$ ($\sim$400 au) ranging from $[\Theta_{obs}]_{400} \sim 0''\!.6$–$3''\!.9$ (i.e., $33°\!.4$–$125°\!.7$ near the source) with a median value $1''\!.64$. The median value of $[\Theta_{obs}]_{400}$ for 19 Class 0 sources is $1''\!.60$, and that for three Class I sources is $2''\!.70$.

3. From the present analysis, the outflow opening angle shows a weak correlation with bolometric temperature in our limited sample observations.

4. The ΔVs exhibit a correlation with $[\Theta_{obs}]_{400}$. As the protostar evolves, the envelope depletes from the polar region, and the cavity opening widens, the outflow material possibly becomes more energetic.

5. The 2D Gaussian fitted 1.3 mm continuum size is found to be reduced in Class I (i.e., beyond the Class 0 to Class I transition region, $T_{bol} = 60$–70 K), which could be due to either varying density profiles depending on power-law indices or envelope dissipation with protostellar evolution. The overall mass distribution of Class 0 (median $\sim$0.13 $M_\odot$) and Class I (median $\sim$0.04 $M_\odot$) also supports the same conclusion.

6. Potential pseudodisks are revealed in 1.3 mm continuum and C^{18}O line emission in some Class 0 sources (e.g., G192.12-11.10). Further investigation in higher spatial and higher velocity resolutions are required to probe the Keplerian rotation.

7. The spectral coverage of this survey incorporates a suite of important diagnostic molecular transitions from the astrochemical perspective. Emission from deuterated species such as N$_2$D$^+$ and DCO$^+$ are detected; this emission serves, for example, as a particularly useful tracer for highlighting the transition from starless to protostellar phases. A subset of protostellar objects with rich features of CH$_3$OH, H$_2$CO, and other COMs like HCOOCH$_3$ and CH$_3$CHO signifies the presence of hot corinos. Broad CO and SiO spectral lines seen toward protostellar sources further delineate active outflows and shocked gas.

This survey provides statistical studies performed to explore the correlation between envelope material, outflow opening angle, and outflow velocity extent with the evolution of protostars. The spectral coverage of these observations can
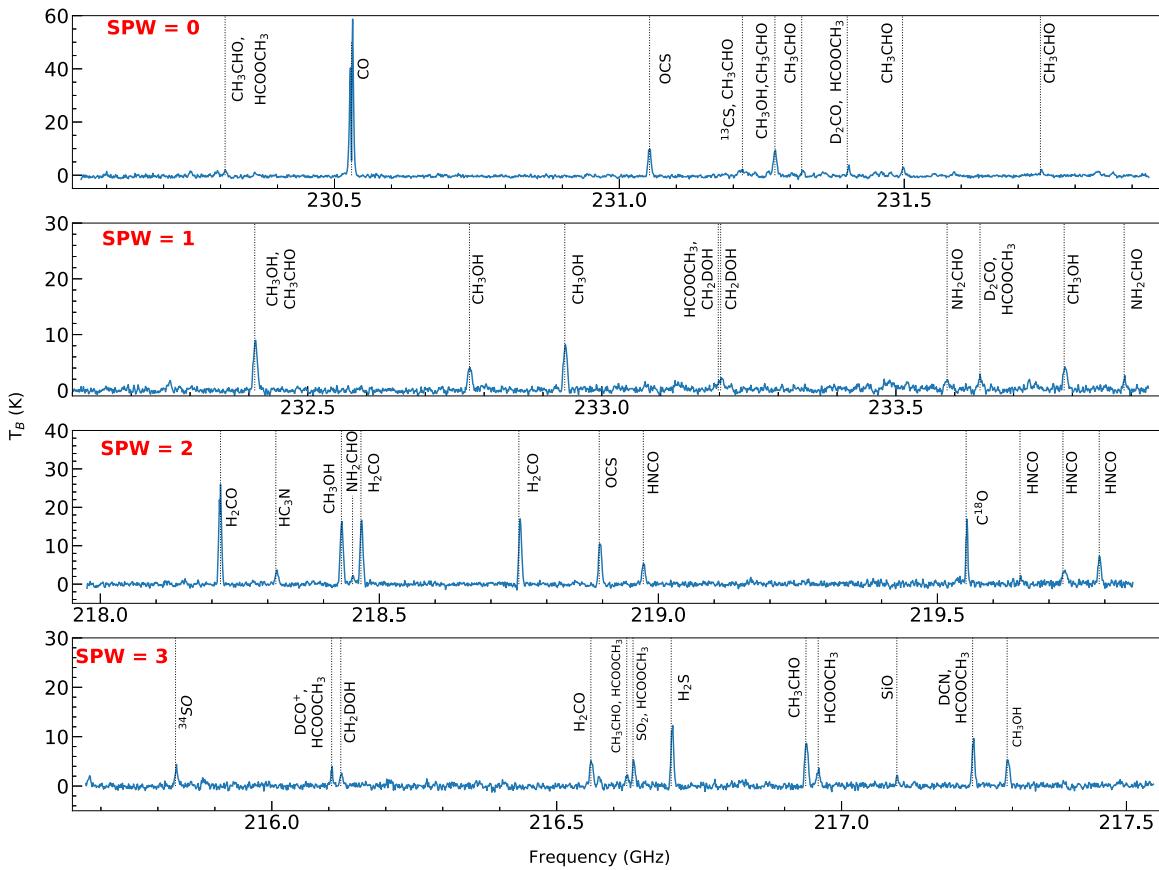
Figure 14. Spectra of a line-rich protostellar object G192.12-11.10 ("hot corino") as identified with 7 m–ACA configuration. All SPWs and line identifications are same as Figure 12.

apprise the astrochemical diagnosis of the molecular species for tracing the transition from starless to protostellar phases. Further high angular and high velocity resolution observations covering different evolutionary stages can apprise these observational findings. In addition, numerical simulations of protostellar outflows launching from variable envelope sizes are definitely required in order to proceed beyond the qualitative hints given by this analysis.

Appendix
TM1+TM2+ ACA Continuum Images

We present the combined continuum maps (TM1+TM2 +ACA) for all the 72 objects in Figures A1–A3 for λ-Orionis, Orion B, and Orion A, respectively. Figure A4 shows the 7 m ACA continuum maps for the nondetected in combined configurations (in Figures A1–A3) and starless dense cores. The velocity-integrated CO maps of outflow structures for all the protostars are displayed in Figure A5.
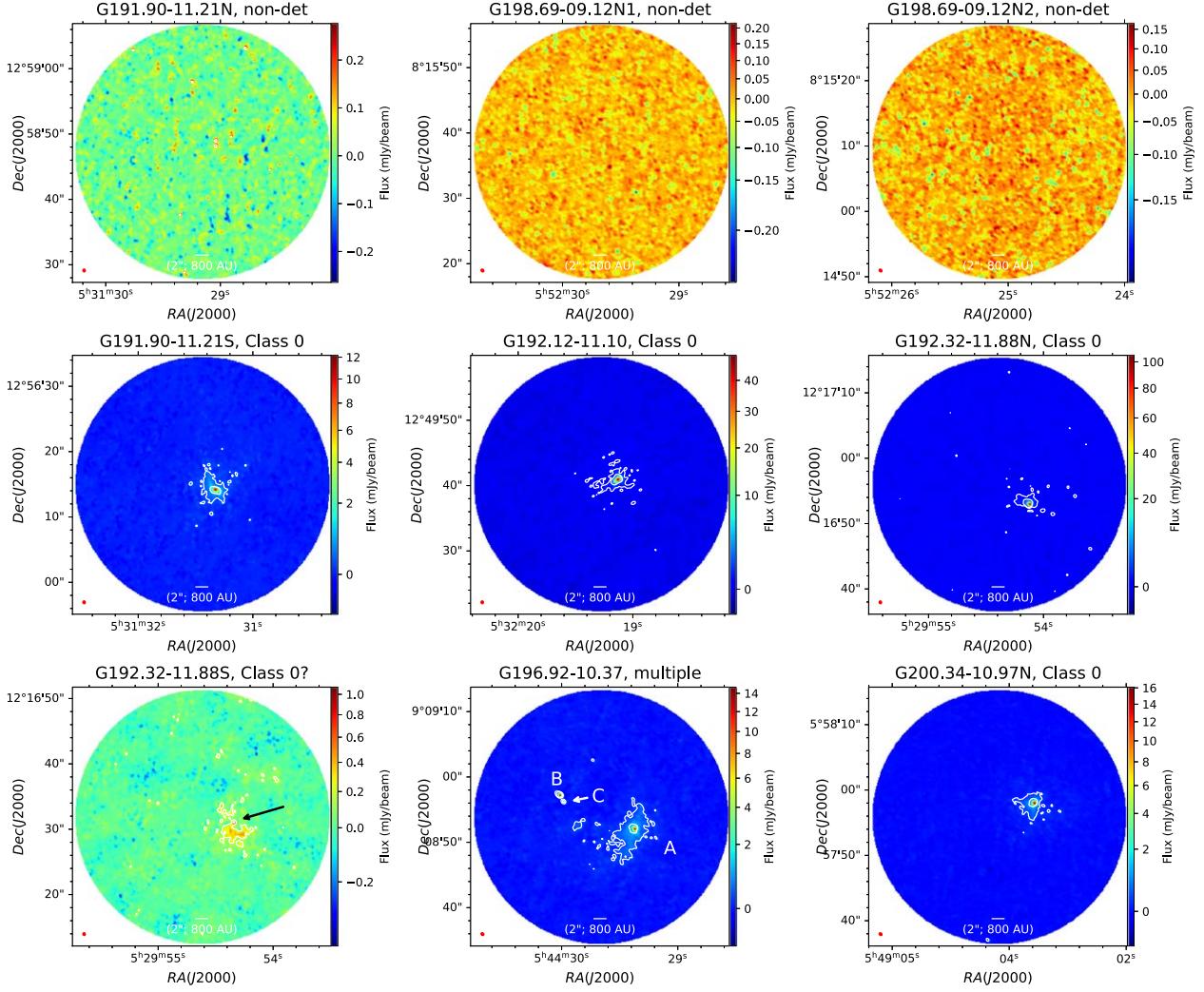
Figure A1. λ-Orionis: Combined TM1, TM2, and 7 m ACA continuum images of nondetected dense cores and Class 0 systems (including multiples). Contours are are at 6 and 30σ, where the corresponding σs are tabulated in Table 1.

Figure A2. Orion B: Combined TM1, TM2, and 7 m ACA continuum images of nondetected, starless dense cores, as well as Class 0 and Class I systems (including multiples). Contours are at 6 and 30σ, where the corresponding σs are tabulated in Table 1.
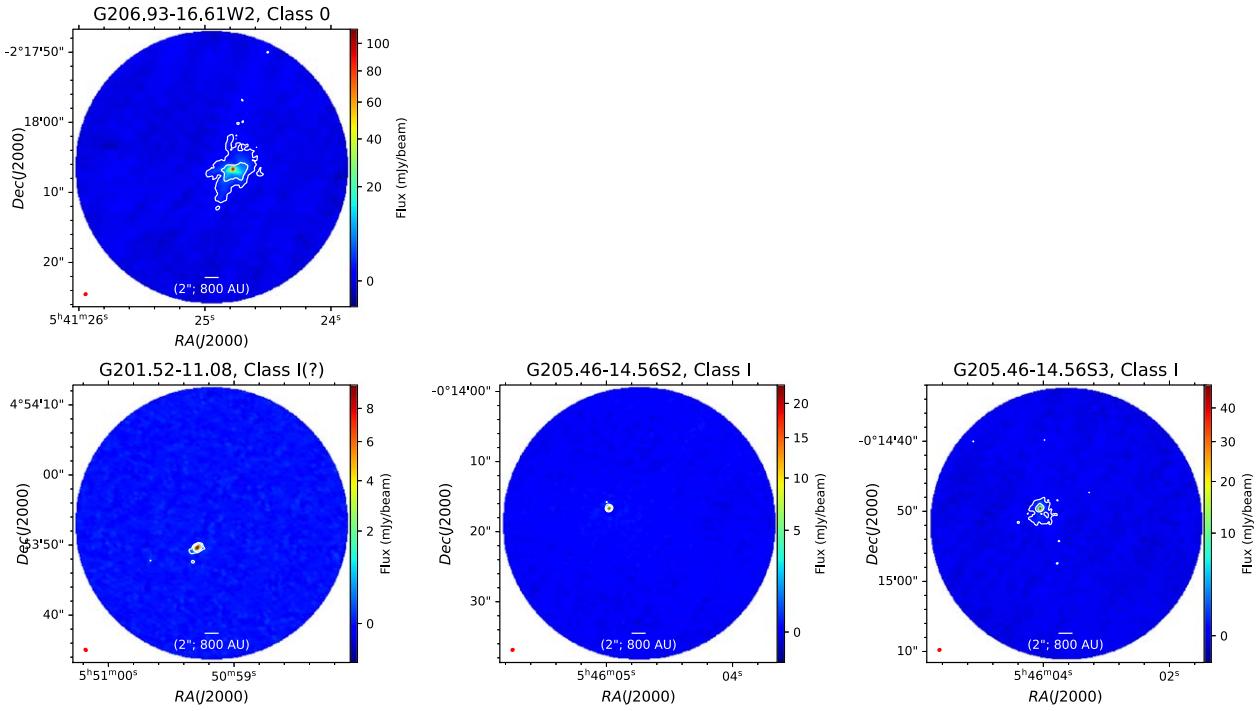
Figure A2. (Continued.)
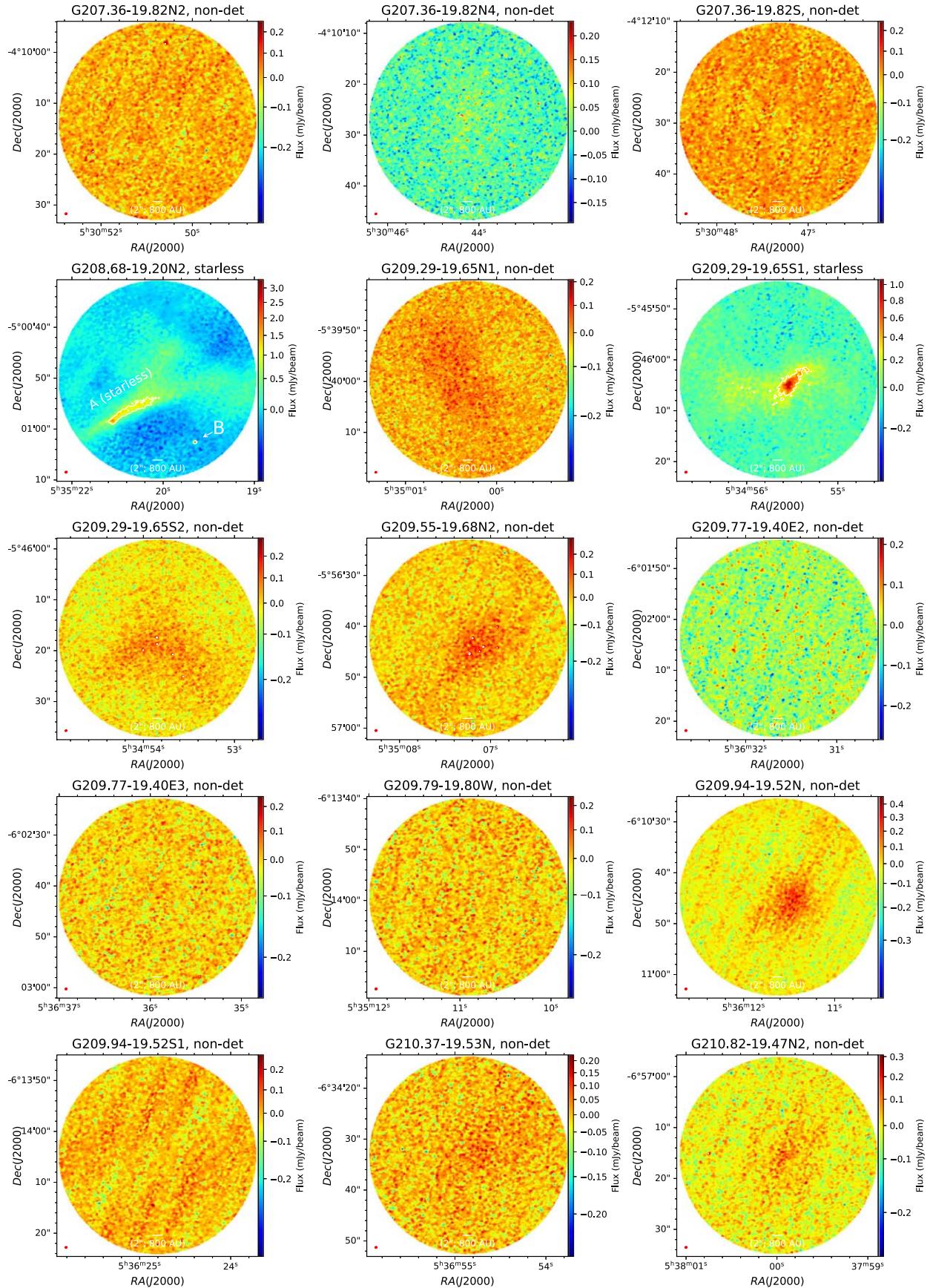
Figure A3. Orion A: Combined TM1, TM2, and 7 m ACA continuum images of nondetected, starless dense cores, as well as Class 0 and Class I systems (including multiples). Contours are are at 6 and 30σ, where the corresponding σs are tabulated in Table 1.
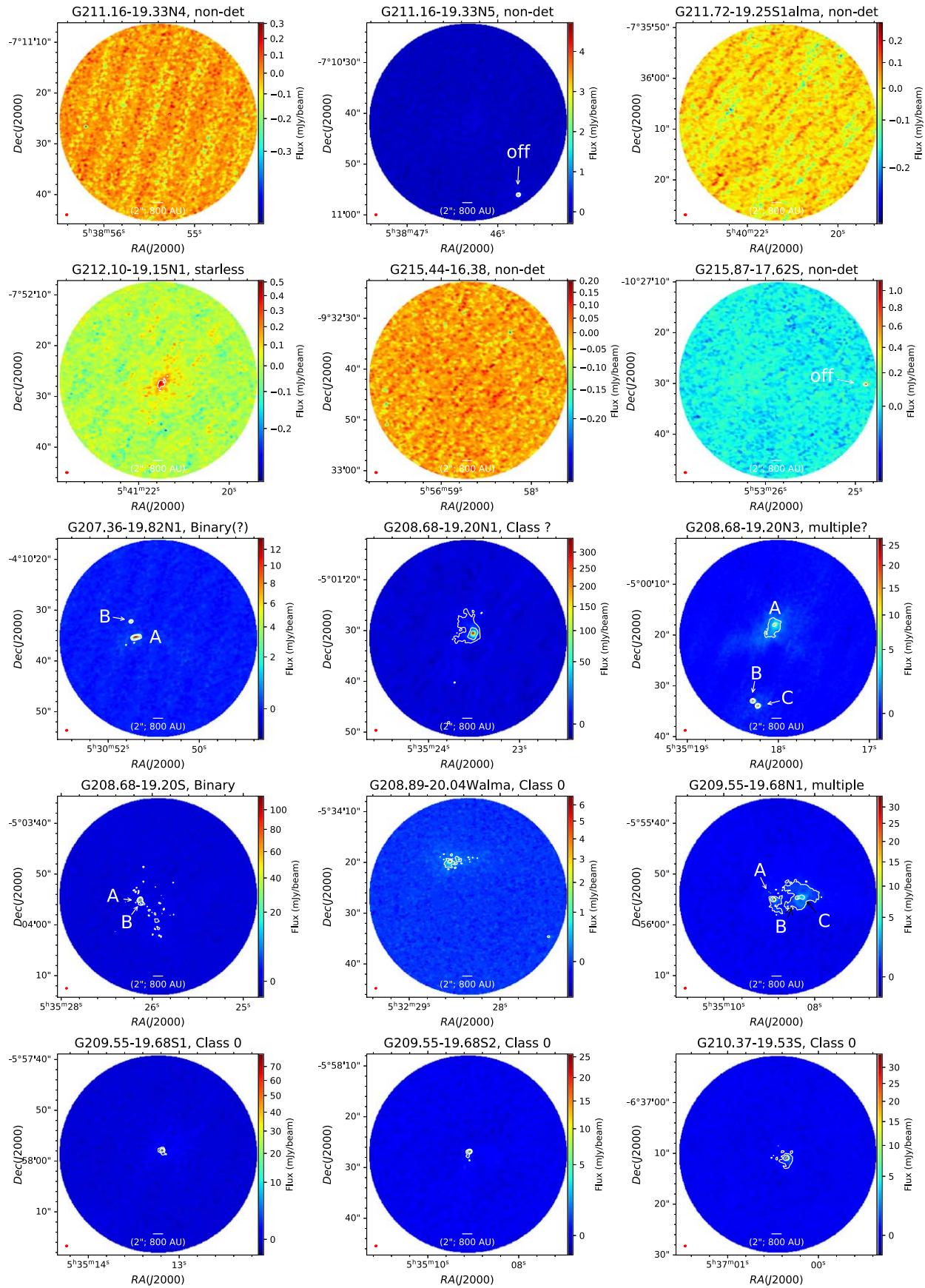
Figure A3. (Continued.)
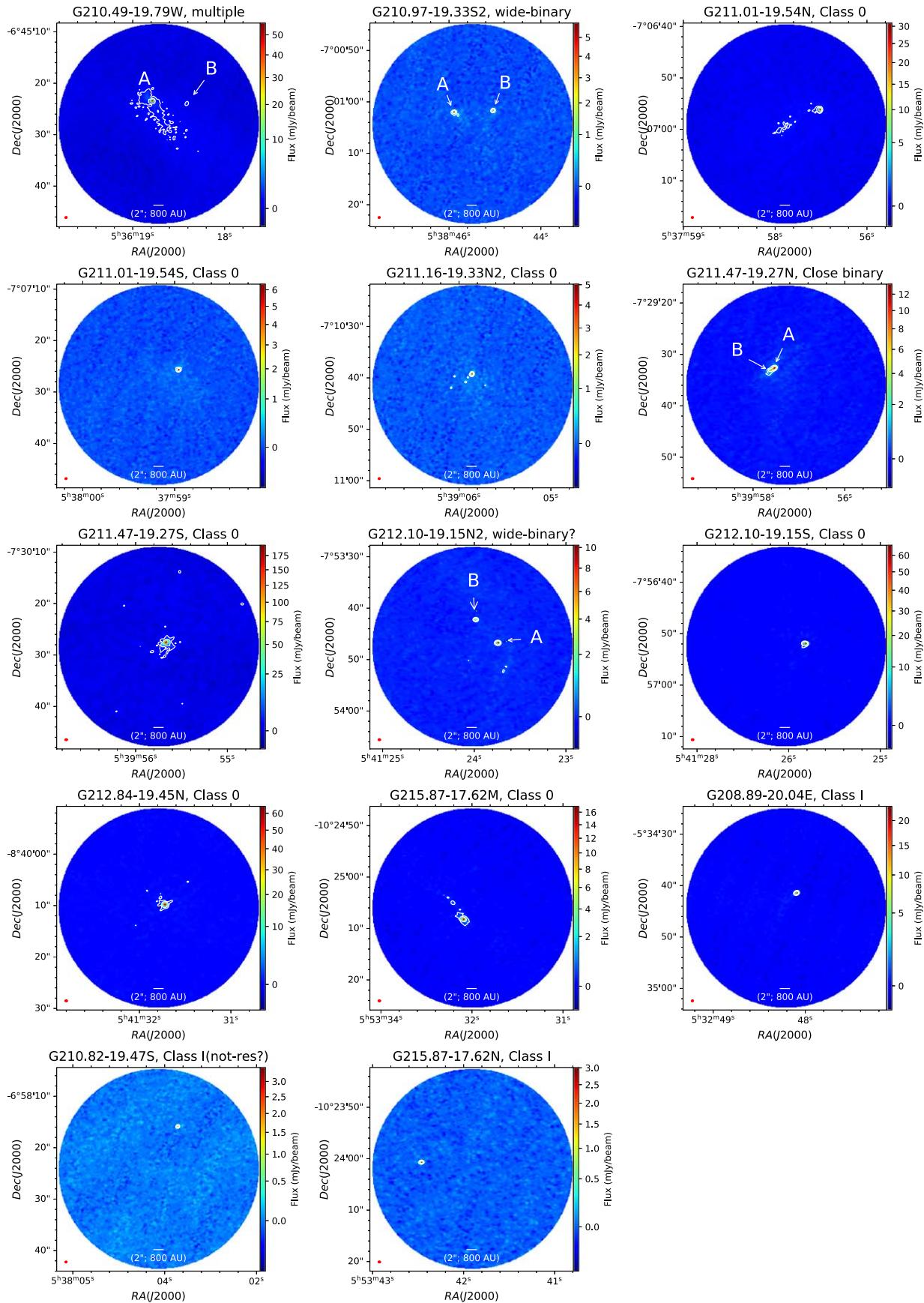
Figure A3. (Continued.)
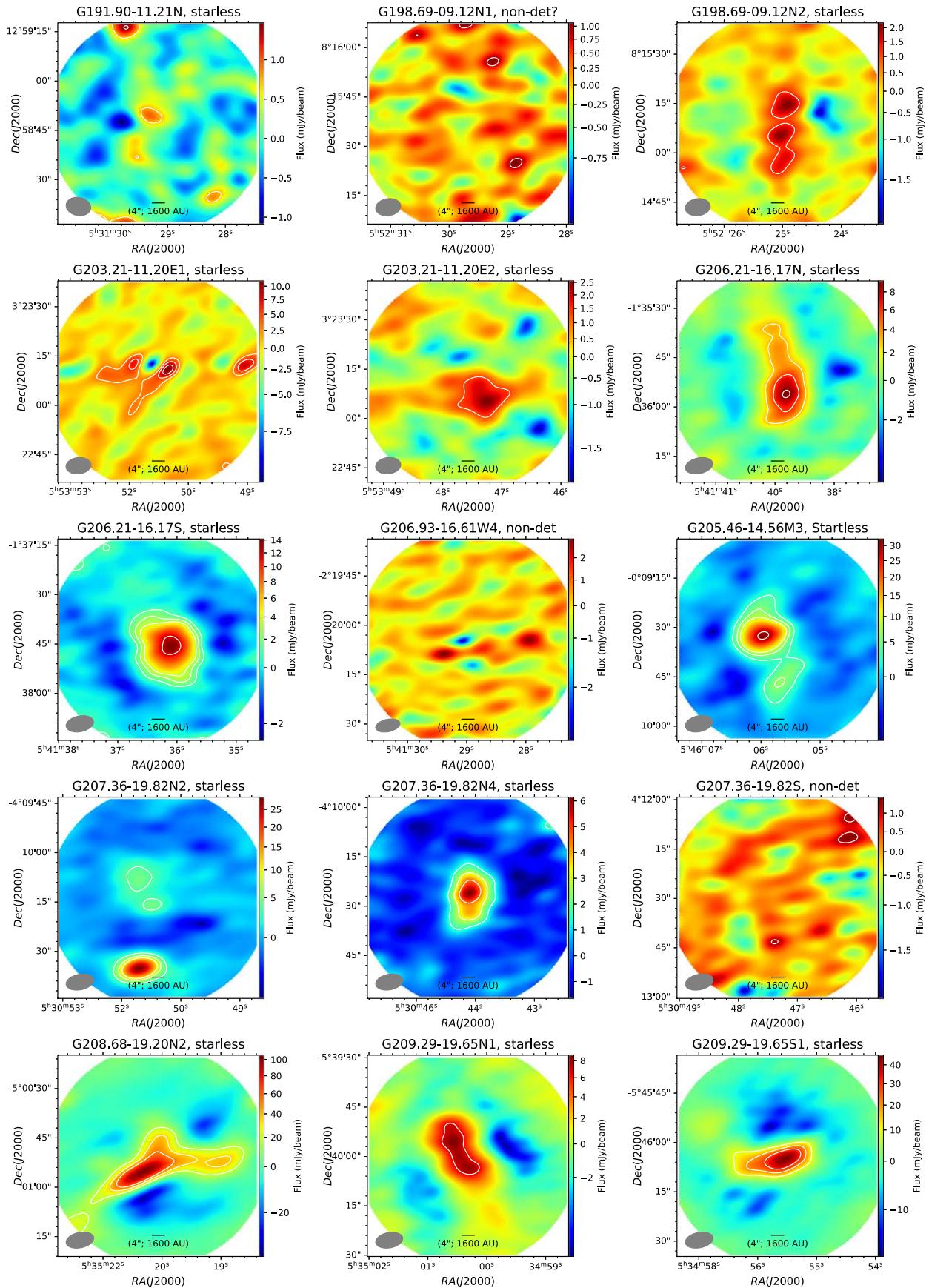
Figure A4. All 7 m ACA continuum maps of nondetected and starless dense cores in combined TM1, TM2, and 7 m ACA continuum images. Contours are are at 3, 6, 9, and 30σ, where the corresponding σs are tabulated in Table 1.
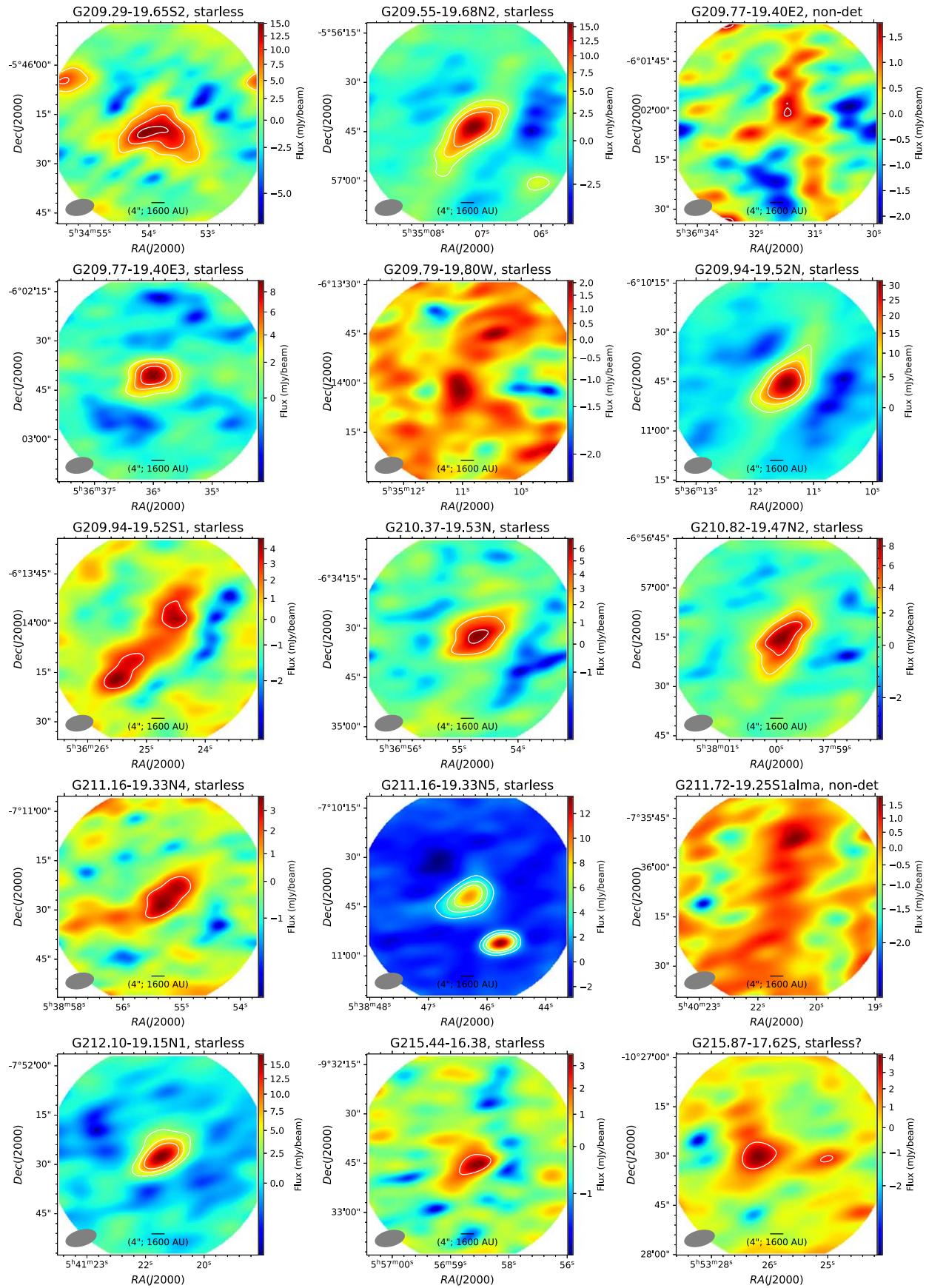
Figure A4. (Continued.)
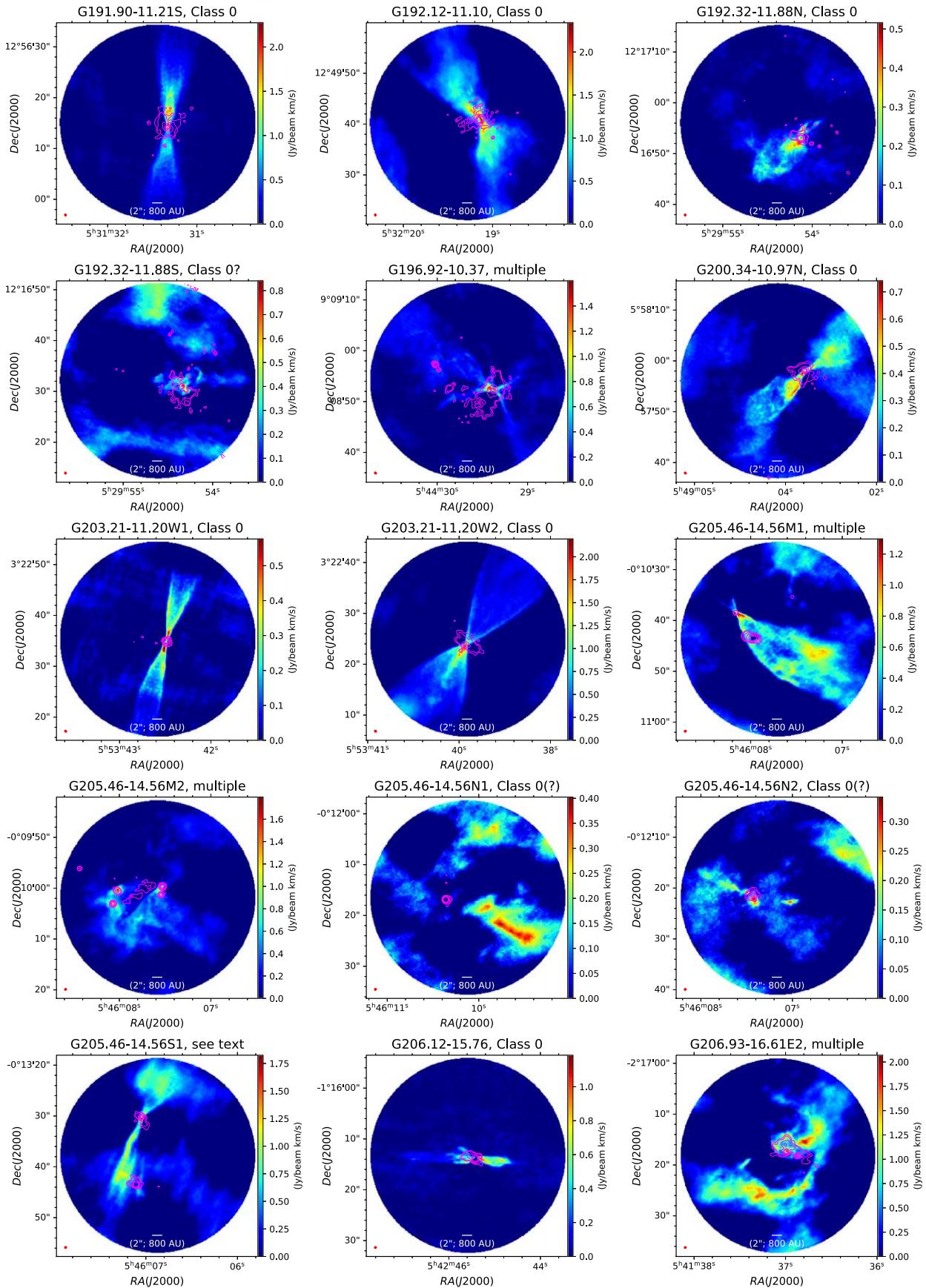
Figure A5. Velocity-integrated CO maps showing outflow structures of the protostellar sources. Magenta contours are 4, 6, 18, 50, 100σ of combined TM1, TM2, and 7 m ACA continuum emission, where the corresponding σs are tabulated in Table 1.
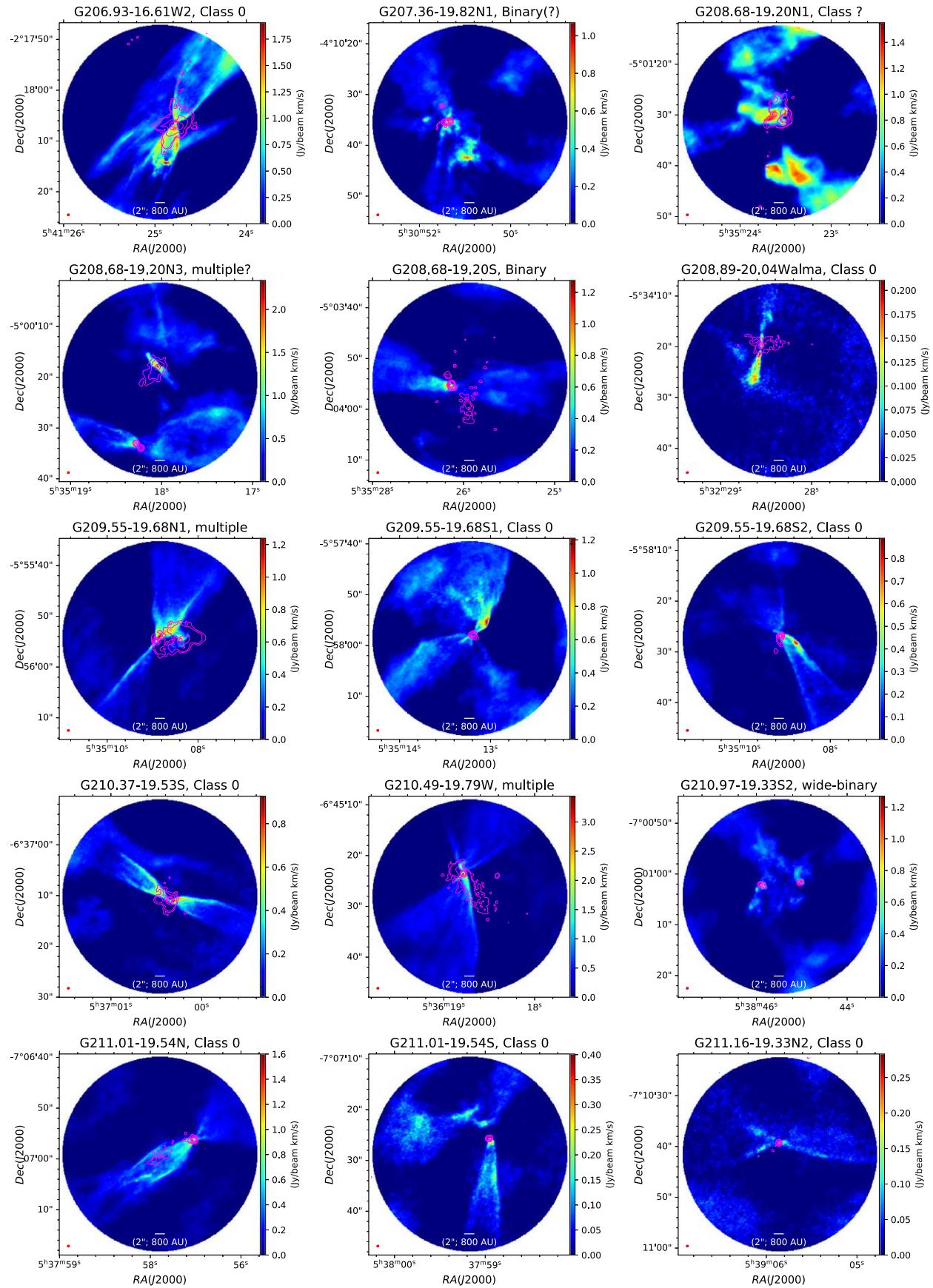
Figure A5. (Continued.)
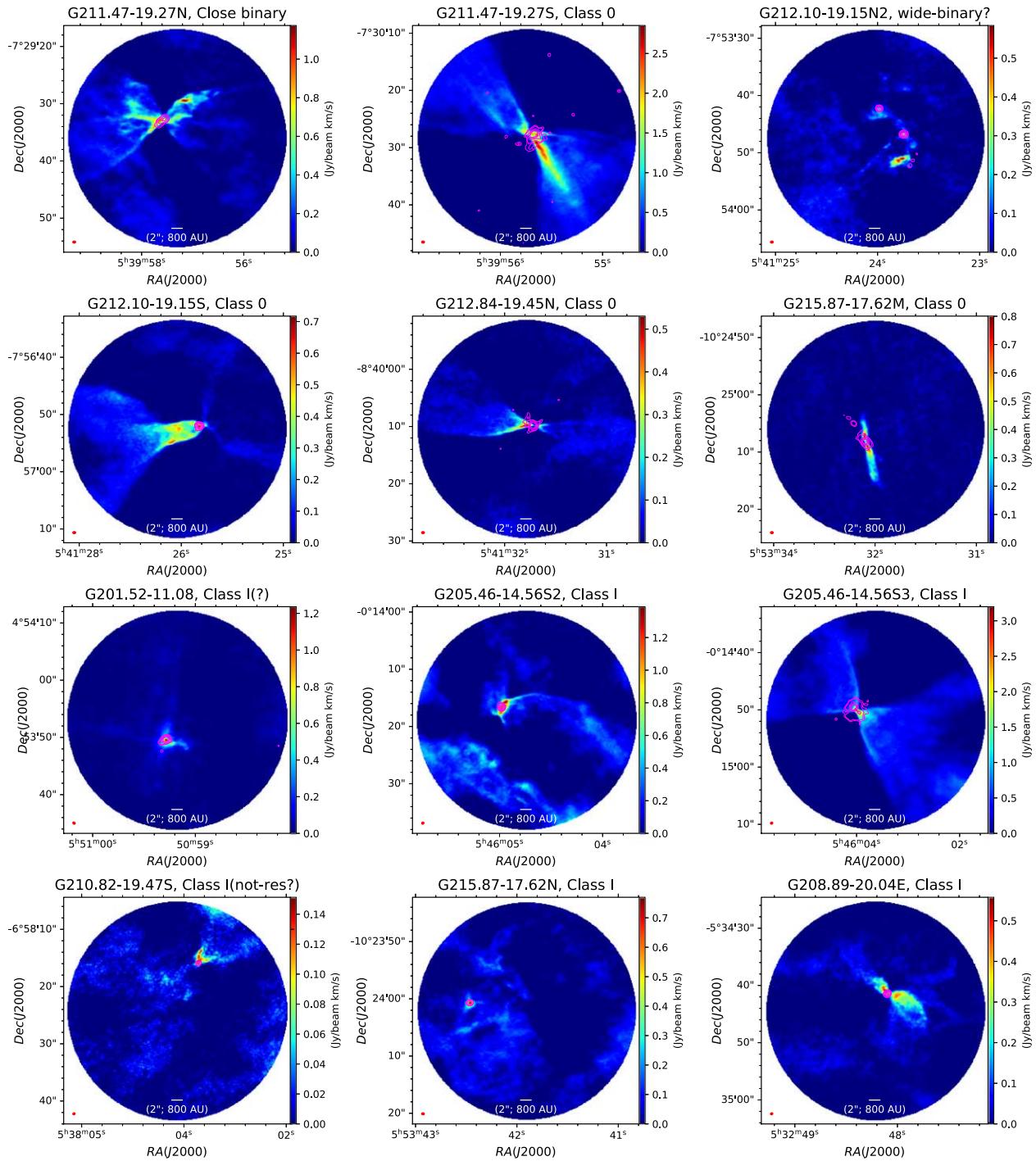
Figure A5. (Continued.)

ORCID iDs

Somnath Dutta ⓘ https://orcid.org/0000-0002-2338-4583
Chin-Fei Lee ⓘ https://orcid.org/0000-0002-3024-5864
Tie Liu ⓘ https://orcid.org/0000-0002-5286-2564
Naomi Hirano ⓘ https://orcid.org/0000-0001-9304-7884
Sheng-Yuan Liu ⓘ https://orcid.org/0000-0003-4603-7119
Ken'ichi Tatematsu ⓘ https://orcid.org/0000-0002-8149-8546
Kee-Tae Kim ⓘ https://orcid.org/0000-0003-2412-7092
Hsien Shang ⓘ https://orcid.org/0000-0001-8385-9838
Dipen Sahu ⓘ https://orcid.org/0000-0002-4393-3463
Gwanjeong Kim ⓘ https://orcid.org/0000-0003-2011-8172
Kai-Syun Jhan ⓘ https://orcid.org/0000-0003-2069-1403
Shih-Ying Hsu ⓘ https://orcid.org/0000-0002-1369-1563
Neal J. Evans ⓘ https://orcid.org/0000-0001-5175-1777
Doug Johnstone ⓘ https://orcid.org/0000-0002-6773-459X
Derek Ward-Thompson ⓘ https://orcid.org/0000-0003-1140-2761
Yi-Jehng Kuan ⓘ https://orcid.org/0000-0002-4336-0730
Chang Won Lee ⓘ https://orcid.org/0000-0002-3179-6334
Jeong-Eun Lee ⓘ https://orcid.org/0000-0003-3119-2087
Mika Juvela ⓘ https://orcid.org/0000-0002-5809-4834
Qizhou Zhang ⓘ https://orcid.org/0000-0003-2384-6589
Patricio Sanhueza ⓘ https://orcid.org/0000-0002-7125-7685
Archana Soam ⓘ https://orcid.org/0000-0002-6386-2906
Woojin Kwon ⓘ https://orcid.org/0000-0003-4022-4132
Leonardo Bronfman ⓘ https://orcid.org/0000-0002-9574-8454
David Eden ⓘ https://orcid.org/0000-0002-5881-3229
Paul F. Goldsmith ⓘ https://orcid.org/0000-0002-6622-8396
Jinhua He ⓘ https://orcid.org/0000-0002-3938-4393
Yuefang Wu ⓘ https://orcid.org/0000-0002-5076-7520
Veli-Matti Pelkonen ⓘ https://orcid.org/0000-0002-8898-1047
Sheng-Li Qin ⓘ https://orcid.org/0000-0003-2302-0613
Shanghuo Li ⓘ https://orcid.org/0000-0003-1275-5251
Di Li ⓘ https://orcid.org/0000-0003-3010-7661

References

Allen, A., Li, Z.-Y., & Shu, F. H. 2003, ApJ, 599, 363
Anglada, G., López, R., Estalella, R., et al. 2007, AJ, 133, 2799
Arce, H. G., & Sargent, A. I. 2006, ApJ, 646, 1070
Arce, H. G., Shepherd, D., Gueth, F., et al. 2007, in Protostars and Planets V, ed. B. Reipurth, D. Jewitt, & K. Keil (Tucson, AZ: Univ. Arizona Press), 245
Aso, Y., Hirano, N., Aikawa, Y., et al. 2019, ApJ, 887, 209
Astropy Collaboration, Price-Whelan, A. M., Sipőcz, B. M., et al. 2018, AJ, 156, 123
Astropy Collaboration, Robitaille, T. P., Tollerud, E. J., et al. 2013, A&A, 558, A33
Bachiller, R., Martin-Pintado, J., & Planesas, P. 1991, A&A, 251, 639
Bachiller, R., & Tafalla, M. 1999, in The Origin of Stars and Planetary Systems, ed. C. J. Lada & N. D. Kylafis (Dordrecht: Kluwer Academic), 227
Bally, J. 2016, ARA&A, 54, 491
Bate, M. R. 1998, ApJL, 508, L95
Beichman, C. A., Myers, P. C., Emerson, J. P., et al. 1986, ApJ, 307, 337
Bergin, E. A., & Tafalla, M. 2007, ARA&A, 45, 339
Beuther, H., & Shepherd, D. 2005, in Cores to Clusters, ed. M. S. N. Kumar, M. Tafalla, & P. Caselli (Cham: Springer), 105
Bontemps, S., Andre, P., Terebey, S., & Cabrit, S. 1996, A&A, 311, 858
Cabrit, S., & Bertout, C. 1992, A&A, 261, 274
Caselli, P., Pineda, J. E., Zhao, B., et al. 2019, ApJ, 874, 89
Ceccarelli, C. 2004, in ASP Conf. Ser. 323, Star Formation in the Interstellar Medium: In Honor of David Hollenbach, ed. D. Johnstone et al. (San Francisco, CA: ASP), 195
Chen, H., Myers, P. C., Ladd, E. F., & Wood, D. O. S. 1995, ApJ, 445, 377
Chen, X., Arce, H. G., Zhang, Q., et al. 2013, ApJ, 768, 110

Codella, C., Bachiller, R., Benedettini, M., et al. 2005, MNRAS, 361, 244
Codella, C., Cabrit, S., Gueth, F., et al. 2014, A&A, 568, L5
Crapsi, A., Caselli, P., Walmsley, M. C., & Tafalla, M. 2007, A&A, 470, 221
Csengeri, T., Leurini, S., Wyrowski, F., et al. 2016, A&A, 586, A149
Cutri, R. M., Skrutskie, M. F., van Dyk, S., et al. 2003, yCat, II/246
Doi, Y., Takita, S., Ootsubo, T., et al. 2015, PASJ, 67, 50
Dunham, M. M., Arce, H. G., Mardones, D., et al. 2014, ApJ, 783, 29
Dunham, M. M., Offner, S. S. R., Pineda, J. E., et al. 2016, ApJ, 823, 160
Dutta, S., Mondal, S., Jose, J., et al. 2015, MNRAS, 454, 3597
Dutta, S., Mondal, S., Samal, M. R., & Jose, J. 2018, ApJ, 864, 154
Eden, D. J., Liu, T., Kim, K.-T., et al. 2019, MNRAS, 485, 2895
Fisher, R. T. 2004, ApJ, 600, 769
Frank, A., Ray, T. P., Cabrit, S., et al. 2014, in Protostars and Planets VI, ed. H. Beuther et al. (Tucson, AZ: Univ. Arizona Press), 451
Furlan, E., Fischer, W. J., Ali, B., et al. 2016, ApJS, 224, 5
Galli, D., Lizano, S., Shu, F. H., & Allen, A. 2006, ApJ, 647, 374
Galli, D., & Shu, F. H. 1993a, ApJ, 417, 243
Galli, D., & Shu, F. H. 1993b, ApJ, 417, 220
Goodwin, S. P., Whitworth, A. P., & Ward-Thompson, D. 2004, A&A, 423, 169
Hartigan, P., Frank, A., Foster, J. M., et al. 2011, ApJ, 736, 29
Hartigan, P., & Hillenbrand, L. 2009, ApJ, 705, 1388
Hsieh, T.-H., Lai, S.-P., & Belloche, A. 2017, AJ, 153, 173
Hsu, S.-Y., Liu, S.-Y., Liu, T., et al. 2020, ApJ, 898, 107
Hunter, J. D. 2007, CSE, 9, 90
Jørgensen, J. K., Hogerheijde, M. R., Blake, G. A., et al. 2004, A&A, 415, 1021
Kim, G., Lee, C. W., Maheswar, G., et al. 2019, ApJS, 240, 18
Kim, G., Tatematsu, K., Liu, T., et al. 2020, ApJS, 249, 33
Kirk, H., Dunham, M. M., Di Francesco, J., et al. 2017, ApJ, 838, 114
Konigl, A., & Pudritz, R. E. 2000, in Protostars and Planets IV, ed. V. Mannings, A. P. Boss, & S. S. Russell (Tucson, AZ: Univ. Arizona Press), 759
Kounkel, M., Covey, K., Suárez, G., et al. 2018, AJ, 156, 84
Kryukova, E., Megeath, S. T., Gutermuth, R. A., et al. 2012, AJ, 144, 31
Kuan, Y.-J., Huang, H.-C., Charnley, S. B., et al. 2004, ApJL, 616, L27
Kuiper, R., Turner, N. J., & Yorke, H. W. 2016, ApJ, 832, 40
Larson, R. B. 1969, MNRAS, 145, 271
Lawrence, A., Warren, S. J., Almaini, O., et al. 2007, MNRAS, 379, 1599
Lee, C.-F. 2020, A&ARv, 28, 1
Lee, C.-F., Kwon, W., Jhan, K.-S., et al. 2019, ApJ, 879, 101
Lee, C.-F., Li, Z.-Y., Hirano, N., et al. 2018, ApJ, 863, 94
Lee, C.-F., Li, Z.-Y., Ho, P. T. P., et al. 2017a, SciA, 3, e1602935
Lee, C.-F., Mundy, L. G., Stone, J. M., & Ostriker, E. C. 2002, ApJ, 576, 294
Lee, J.-E., Lee, S., Dunham, M. M., et al. 2017b, NatAs, 1, 0172
Li, S., Wang, J., Fang, M., et al. 2019, ApJ, 878, 29
Liu, C.-F., & Shang, H. 2012, ApJ, 761, 94
Liu, T., Kim, K.-T., Juvela, M., et al. 2018, ApJS, 234, 28
Liu, T., Zhang, Q., Kim, K.-T., et al. 2016, ApJS, 222, 7
Louvet, F., Motte, F., Gusdorf, A., et al. 2016, A&A, 595, A122
Machida, M. N., & Basu, S. 2019, ApJ, 876, 149
Machida, M. N., Inutsuka, S.-i., & Matsumoto, T. 2014, MNRAS, 438, 2278
Maret, S., Ceccarelli, C., Tielens, A. G. G. M., et al. 2005, A&A, 442, 527
Masunaga, H., & Inutsuka, S.-i. 2000, ApJ, 531, 350
McMullin, J. P., Waters, B., Schiebel, D., Young, W., & Golap, K. 2007, in ASP Conf. Ser. 376, CASA Architecture and Applications, ed. R. A. Shaw, F. Hill, & D. J. Bell (San Francisco, CA: ASP), 127
Megeath, S. T., Gutermuth, R., Muzerolle, J., et al. 2012, AJ, 144, 192
Murillo, N. M., Lai, S.-P., Bruderer, S., Harsono, D., & van Dishoeck, E. F. 2013, A&A, 560, A103
Myers, P. C., & Benson, P. J. 1983, ApJ, 266, 309
Myers, P. C., & Ladd, E. F. 1993, ApJL, 413, L47
Nony, T., Motte, F., Louvet, F., et al. 2020, A&A, 636, A38
Offner, S. S. R., Kratter, K. M., Matzner, C. D., Krumholz, M. R., & Klein, R. I. 2010, ApJ, 725, 1485
Ohashi, N., Saigo, K., Aso, Y., et al. 2014, ApJ, 796, 131
Ohashi, S., Sanhueza, P., Sakai, N., et al. 2018, ApJ, 856, 147
Ossenkopf, V., & Henning, T. 1994, A&A, 291, 943
Padoan, P., & Nordlund, Å. 2002, ApJ, 576, 870
Pesenti, N., Dougados, C., Cabrit, S., et al. 2004, A&A, 416, L9
Planck Collaboration, Ade, P. A. R., Aghanim, N., et al. 2016, A&A, 594, A28
Pyo, T.-S., Hayashi, M., Kobayashi, N., et al. 2006, ApJ, 649, 836
Reipurth, B., & Bally, J. 2001, ARA&A, 39, 403
Richer, J. S., Shepherd, D. S., Cabrit, S., Bachiller, R., & Churchwell, E. 2000, in Protostars and Planets IV, ed. V. Mannings, A. P. Boss, & S. S. Russell (Tucson, AZ: Univ. Arizona Press), 867

Schnee, S., Di Francesco, J., Enoch, M., et al. 2012, ApJ, 745, 18
Schnee, S., Enoch, M., Johnstone, D., et al. 2010, ApJ, 718, 306
Seale, J. P., & Looney, L. W. 2008, ApJ, 675, 427
Shang, H., Allen, A., Li, Z.-Y., et al. 2006, ApJ, 649, 845
Shang, H., Shu, F. H., & Glassgold, A. E. 1998, ApJL, 493, L91
Shu, F. H., Najita, J. R., Shang, H., & Li, Z. Y. 2000, in Protostars and Planets
    IV, ed. V. Mannings, A. P. Boss, & S. S. Russell (Tucson, AZ: Univ.
    Arizona Press), 789
Sipilä, O., Caselli, P., Redaelli, E., Juvela, M., & Bizzocchi, L. 2019, MNRAS,
    487, 1269
Snell, R. L., Loren, R. B., & Plambeck, R. L. 1980, ApJL, 239, L17
Stutz, A. M., Tobin, J. J., Stanke, T., et al. 2013, ApJ, 767, 36
Tatematsu, K., Liu, T., Kim, G., et al. 2020, ApJ, 895, 119
Tobin, J. J., Bourke, T. L., Mader, S., et al. 2019, ApJ, 870, 81
Tychoniec, Ł., Tobin, J. J., Karska, A., et al. 2018, ApJS, 238, 19
Tobin, J. J., Kratter, K. M., Persson, M. V., et al. 2016a, Natur, 538, 483
Tobin, J. J., Looney, L. W., Li, Z.-Y., et al. 2016b, ApJ, 818, 73

Tobin, J. J., Sheehan, P. D., Megeath, S. T., et al. 2020, ApJ, 890, 130
Tobin, J. J., Stutz, A. M., Megeath, S. T., et al. 2015, ApJ, 798, 128
Tokuda, K., Fujishiro, K., Tachihara, K., et al. 2020, ApJ, 899, 10
Tomisaka, K. 2002, ApJ, 575, 306
van Kempen, T. A., van Dishoeck, E. F., Güsten, R., et al. 2009, A&A,
    501, 633
Velusamy, T., Langer, W. D., & Thompson, T. 2014, ApJ, 783, 6
Wang, L.-Y., Shang, H., Su, Y.-N., et al. 2014, ApJ, 780, 49
Ward-Thompson, D., Pattle, K., Kirk, J. M., et al. 2016, MNRAS, 463,
    1008
Williams, J. P., Blitz, L., & McKee, C. F. 2000, in Protostars and Planets IV,
    ed. V. Mannings, A. P. Boss, & S. S. Russell (Tucson, AZ: Univ. Arizona
    Press), 97
Wright, E. L., Eisenhardt, P. R. M., Mainzer, A. K., et al. 2010, AJ, 140, 1868
Yi, H.-W., Lee, J.-E., Liu, T., et al. 2018, ApJS, 236, 51
Yıldız, U. A., Kristensen, L. E., van Dishoeck, E. F., et al. 2015, A&A,
    576, A109